J. Fluid Mech. (2011), *vol.* 686, *pp.* 77–108. © Cambridge University Press 2011
doi:10.1017/jfm.2011.284

Dynamic bifurcations and pattern formation in melting-boundary convection

G. M. Vasil[1,2]† and M. R. E. Proctor[3]

[1] Canadian Institute for Theoretical Astrophysics, 60 St George Street, Toronto, ON M5S 3H8, Canada

[2] JILA, University of Colorado, Boulder, CO 80309-0440, USA

[3] Department of Applied Mathematics & Theoretical Physics, University of Cambridge, Cambridge CB3 0WA, UK

(Received 8 November 2010; revised 7 April 2011; accepted 27 June 2011; first published online 23 September 2011)

We consider weakly nonlinear convection in a fluid layer with a melting top boundary. This leads us to derive a new set of non-autonomous envelope equations as a dynamic generalization to the well-known Ginzburg–Landau equation. However, this new system possesses a number of interesting properties not found in systems close to a traditional dynamic bifurcation, because it involves the interaction of two destabilizing mechanisms. We investigate the system both analytically and numerically; specifically, we find the robust 'locking in' of spatially complex patterns, and show this is a general feature of systems of this nature.

Key words: buoyancy-driven instability, morphological instability, solidification/melting

1. Introduction

Dynamical systems exhibiting phase transitions and heat transport are ubiquitous in both nature and applications (Huppert 2000; Worster 2000). Systems where a phase transition takes place at a well-defined dynamical interface generally fall into a category called Stefan problems. Given that many Stefan problems involve liquid–solid phase transitions, it is also natural that heat transport in the liquid component of such systems often involves buoyancy and convection. It is therefore the purpose of our current investigation to consider some of the dynamical consequences that follow from a system that possesses both buoyant convective heat transport and liquid–solid phase transitions.

The theory of stability in traditional Rayleigh–Bénard systems has been well understood for quite some time (Chandrasekhar 1961). Typically with regard to the manner in which mathematical analysis is conducted, the stability of a dynamical system (with Rayleigh–Bénard convection furnishing a good example) is an either/or proposition. Conceptually a system is considered with a pre-determined set of parameters (e.g. strength of gravity, type of fluid, degree of thermal forcing, and domain geometry/size) and one then asks whether or not the system is stable or unstable given that set of fixed parameters. In practice, a system is rarely ever built merely as either stable or unstable with a fixed set of parameters. Rather, it is often

† Email address for correspondence: vasil@cita.utoronto.ca

https://doi.org/10.1017/jfm.2011.284 Published online by Cambridge University Press

the case that an experimenter builds a system with a subset of important parameters fixed in a permanent manner (e.g. type of fluid) and leaves one or more remaining parameters (e.g. degree of thermal forcing) as variables that may be adjusted time-dependently to produce the desired stable/unstable configuration.

This distinction is not merely a trivial matter. It implies that often a system is initially constructed as stable and is then slowly evolved to an unstable state in an inherently time-dependent fashion. This often-unavoidable fact implies that, near transitions, many systems may behave differently from what is expected based on traditional eigen-analysis; see Benoît (1990) and articles within for a thorough introduction. Early related work by Foster (1965) considers the stability of a layer that is time-dependently cooled from above at a uniform rate. Mandel & Erneux (1987) and Lythe (1996) consider the effects of time dependence in the class of pitchfork bifurcations (including Rayleigh–Bénard systems) and found that delay of onset was one particularly notable feature when including the presence of noise. Thus far however, the study of dynamic bifurcations mainly centres around systems in which the critical parameter is still an externally chosen variable, such as an experimenter slowly increasing the temperature difference across a Rayleigh–Bénard layer. Or, in systems where feedbacks are allowed onto the bifurcation parameter, the underlying system is often considered as an ordinary differential system, and the bifurcation parameter is spatially homogeneous (Benoît 1990). There is another interesting class of systems where the bifurcation parameter is a variable that is internal to the system's dynamics, which can undergo spatial modulations. This leads us to consider Stefan-type systems where the system's geometry need not be fixed in advance if one or more boundaries are allowed to undergo phase transitions as a result of heat transport within the interior.

The work of Davis, Müller & Dietsche (1984) is an excellent starting point in studying the naturally intertwined nature of Stefan systems and convection. In that work, the authors consider a layer of liquid melt lying below a layer of the same substance in its solid form. Specifically, they consider instabilities about a formal equilibrium state, which is provided by the ability of the top solid to conduct heat away from the fluid. Here we consider a system that is very similar to that in Davis *et al.* (1984) but where the top boundary is held at its melting temperature. This feature does not allow for formal equilibria, but leads to an inherently time-dependent background state in which the underlying fluid layer slowly deepens and hence becomes less stable to convection.

Below, we derive a set of dynamical equations describing the amplitude of fluid convection and surface interface deformations in a deepening layer with melting top boundary. Our eventual system resembles the well-known Ginzburg–Landau (GL) equation (Cross & Hohenberg 1993) with a couple of significant differences. First, because we are considering the stability of an inherently time-dependent background state, our derived amplitude equations necessarily contain time-dependent coefficients. Second, given the possibility for non-trivial morphological changes in the meltable liquid–solid interface, our derived system also contains a separate equation describing a coupled morphological mode. Both of these two features provide interesting new behaviour in comparison with a steady, non-melting system.

https://doi.org/10.1017/jfm.2011.284 Published online by Cambridge University Press

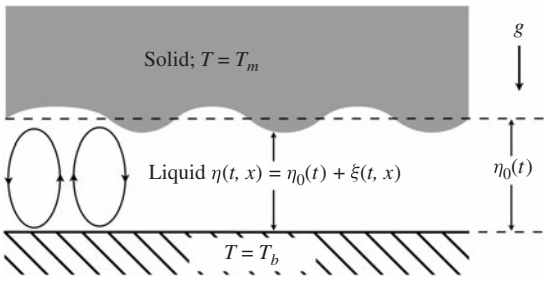


FIGURE 1. Diagram of the basic domain parameters and problem setup. The bottom boundary is held at a fixed temperature, T_b. The top boundary is composed of a large region of meltable substance that is held at its melting temperature, T_m. The region between the top and bottom boundaries consists of a fluid melt, which can become unstable because of gravity, g, in the downward direction.

2. Formulation

2.1. *Fundamental equations and dimensionless scalings*

The basic governing (dimensionless) equations under consideration are the Boussinesq equations (Spiegel & Veronis 1960; Chandrasekhar 1961), i.e.

$$\frac{1}{Pr}(\partial_t + \boldsymbol{u}\cdot\nabla)\boldsymbol{u} + \nabla P = Ra\,T\hat{\boldsymbol{z}} + \Delta\boldsymbol{u}, \tag{2.1}$$

$$\nabla\cdot\boldsymbol{u} = 0, \tag{2.2}$$

$$(\partial_t + \boldsymbol{u}\cdot\nabla)T = \Delta T, \tag{2.3}$$

with the non-dimensional Rayleigh and Prandtl numbers, respectively,

$$Ra = \frac{g\alpha(T_b - T_m)H_0^3}{\nu\kappa}, \quad Pr = \frac{\nu}{\kappa}. \tag{2.4}$$

The system (2.1)–(2.3) determines the velocity, $\boldsymbol{u} = (u, v, w)$, and temperature, T, of a liquid that occupies an extended layer contained between $0 < z < \eta(t, x, y)$; see figure 1. The various parameters in (2.4) express their usual meaning, where g is gravity, $\alpha = -(\partial \ln\rho/\partial T)|_{\rho_0,T_0}$ is the thermal expansion coefficient, ν is the kinematic viscosity, and κ is the thermal diffusivity, $T_b - T_m$ is a characteristic temperature difference across the layer, and H_0 is a characteristic layer depth (described in greater detail below). Specifically, all of these quantities are properties of the liquid only, as opposed to the solid boundaries.

Since our model is formulated as an initial-value problem, and since we use a handful of different time scales, some care is required when discussing the appropriate length and time scales used to scale our dynamical equations. We start off with a layer of constant depth and allow it to deepen as the top boundary melts. Eventually, the layer depth is sufficient to allow buoyancy-driven instability and the system bifurcates to a state of lower symmetry. We denote the initial depth by $\eta(t = 0) = H_0$, which is the convenient characteristic length scale that we use as our unit of length. Furthermore, H_0 in conjunction with the thermal diffusivity, κ, provides a natural velocity scale, κ/H_0 with which to non-dimensionalize $\boldsymbol{u}$. The ratio H_0^2/κ gives the natural time unit used to scale (2.1)–(2.3). However, in our analysis we find it necessary to use an array of different time scales, depending on the situation. It is

https://doi.org/10.1017/jfm.2011.284 Published online by Cambridge University Press

therefore helpful to define the non-dimensional Strouhal number

$$St = \frac{H_0^2}{\kappa t_0}, \tag{2.5}$$

where t_0 is a general characteristic time unit that can be used as an alternative to H_0^2/κ for scaling our dynamical equations. Note that (2.1)–(2.3) correspond to $St = 1$, but this changes as we progress. Also, in later sections, we use the notation t^* when referring to the original thermal-diffusion scale time variable.

Much of the interest in this system lies in the dynamical boundary conditions. The heated non-melting bottom boundary at $z = 0$ is considered no-slip, and perfectly conducting, i.e.

$$\boldsymbol{u}|_{z=0} = \boldsymbol{0}, \quad T|_{z=0} = T_b, \tag{2.6}$$

although other possibilities for this boundary exist (e.g. stress-free and/or fixed-thermal-flux). The top boundary is a meltable solid substance that is held at its melting temperature, T_m. We set the melting temperature to zero without loss of generality (i.e. $T_m = 0$), and since we want our top boundary to melt, we require $T_b > T_m$. Therefore, we set our units of temperature in terms of the difference across the layer (i.e. $T_b - T_m = 1$).

In dimensional form, the dynamical top boundary condition at $z = \eta(t, x, y)$ consists of the Stefan and melting conditions (Woods 1992; Worster 2000), i.e.

$$T|_{z=\eta} = T_m, \quad L\partial_t \eta = -c_p \kappa \hat{\boldsymbol{n}} \cdot \boldsymbol{\nabla} T|_{z=\eta}, \tag{2.7}$$

where L is the latent heat of fusion/melting, c_p is the specific heat capacity at constant pressure of the liquid, and $\hat{\boldsymbol{n}}$ is the unit normal to the surface, $\eta(t, x, y)$, and is pointing into the solid. That is,

$$\hat{\boldsymbol{n}} = \frac{\boldsymbol{\nabla}(z - \eta)}{|\boldsymbol{\nabla}(z - \eta)|} = \hat{\boldsymbol{z}} - \boldsymbol{\nabla}\eta + O(|\boldsymbol{\nabla}\eta|^2). \tag{2.8}$$

In (2.7), we could include the Gibbs–Thompson effect due to the surface energy of the solid–liquid interface (Worster 2000). However, for the dynamical scales of interest (i.e. convective length scales), the Gibbs–Thompson effect amounts to an extremely small ($\sim 10^{-9}$) adjustment to the coefficients in our eventual dynamical equations, and is therefore neglected.

In the Stefan condition (2.7), we assume that the density of the solid and the density of the melt are equal. This is not strictly true for many substances, but also serves as a convenient simplification. The one place that this simplification might make a difference is in normal-flow boundary condition at the melting boundary. However, the normal flow at the melting boundary is proportional to the rate of melting, $\hat{\boldsymbol{n}} \cdot \boldsymbol{u} \sim \partial_t \eta$ (Davis *et al.* 1984), and because we are examining dynamics in the slowly melting regime, it happens that the normal-flow contribution does not enter at the relevant order, and can be formally neglected. Therefore, the top boundary is effectively no-slip and so we take

$$\boldsymbol{u}|_{z=\eta} = \boldsymbol{0}. \tag{2.9}$$

After rescaling according to the same length and time scales used in (2.1)–(2.3), the Stefan condition now takes the form

$$S\partial_t \eta + \hat{\boldsymbol{n}} \cdot \boldsymbol{\nabla} T|_{z=\eta} = 0. \tag{2.10}$$

https://doi.org/10.1017/jfm.2011.284 Published online by Cambridge University Press

There is now a new dimensionless quantity, the Stefan number S (Worster 2000), which controls the rate of melting and is given by

$$S = \frac{L}{c_p(T_b - T_m)}. \tag{2.11}$$

In the following analysis, we are mostly interested in the large-Stefan-number limit, $S \gg 1$, i.e. we are interested in a slowly melting top boundary. From (2.10) we see that if we divide by S and take $S \to \infty$, then we would find $\partial_t \eta = 0$, and the depth of the layer would not change. Our aim is a reduced system in the limit where the top boundary is slowly moving, and when the time scale of this melting is similar to weakly nonlinear buoyancy time scales.

2.2. *Basic state*

The following analysis is similar to that outlined in Worster (2000) for solidification, as opposed to melting, and is a special case of that considered in Woods (1992). Eventually, we focus on the large-Stefan-number limit and the effects of fluid motion. For now, we consider arbitrary Stefan number and no fluid motion, i.e. $\boldsymbol{u} = \boldsymbol{0}$. Furthermore, (for now) we only allow variation in the vertical direction, i.e. $\partial_x = \partial_y = 0$. These assumptions imply the following simplified balances:

$$\partial_t T = \partial_z^2 T, \quad S\partial_t \eta = -\partial_z T|_{z=\eta}, \quad \partial_z P = Ra\, T. \tag{2.12}$$

With the simplifications, (2.12) admits a similarity solution of the form

$$T(t, z) = 1 - \frac{\operatorname{erf}(\alpha z/\eta(t))}{\operatorname{erf}(\alpha)}, \quad \eta(t) = \sqrt{4\alpha^2 t + 1}, \tag{2.13}$$

where α is an as yet undetermined parameter, and erf is the error function given by

$$\operatorname{erf}(\zeta) = \frac{2}{\sqrt{\pi}} \int_0^{\zeta} \mathrm{e}^{-\zeta_0^2}\, \mathrm{d}\zeta_0. \tag{2.14}$$

Substituting (2.13) into the Stefan condition (2.12) gives

$$\frac{1}{S} = \sqrt{\pi}\, \alpha \operatorname{erf}(\alpha) \exp(\alpha^2). \tag{2.15}$$

For any given value of S, this transcendental relation is easily solved numerically; see figure 2. However, for $S \gg 1$ we expand the right-hand side of (2.15) and obtain

$$\frac{1}{S} = 2\alpha^2 + O(\alpha^4). \tag{2.16}$$

Given (2.16), for large Stefan number, the background temperature profile simplifies greatly, i.e.

$$T(t, z) = 1 - \frac{z}{\eta(t)} + O(S^{-1}), \quad \eta(t) = \sqrt{\frac{2t}{S} + 1} + O\left(\frac{t}{S^2}\right). \tag{2.17}$$

The motivation for not expanding (2.17) entirely in terms of S^{-1} is because of the non-uniformity in time. That is, since time multiplies S^{-1}, the asymptotic form of $\eta(t)$ depends strongly on what time scale we choose to examine the dynamics. Nevertheless, the linear profile (2.17) remains valid regardless of what form we take for $\eta(t)$.

https://doi.org/10.1017/jfm.2011.284 Published online by Cambridge University Press

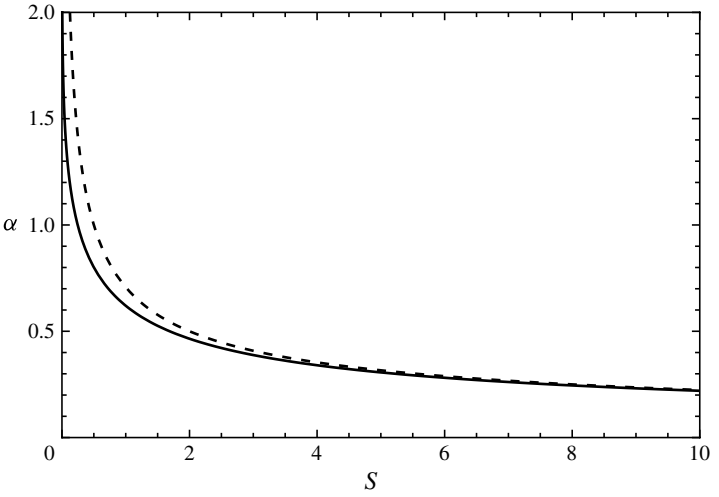


FIGURE 2. The solid curve shows the melting parameter, α, versus Stefan number, S, given by the expression (2.15). The dashed curve shows the asymptotic approximation given by (2.16). In the large-Stefan-number regime, the two curves agree quite well.

3. Nonlinear asymptotic analysis

In this section we derive a set of (Ginzburg–Landau-type) envelope equations for convection in a slowly expanding domain. It happens that the procedure of derivation and the eventual answer are very similar to the reduction of traditional Rayleigh–Bénard convection near onset (Newell & Whitehead 1969; Segel 1969; Cross 1980). We are mainly interested in how to derive the novel terms in the dynamical equations, and are not particularly interested in the standard derivation of envelope equations in their generality. Therefore, in this section, we simplify the problem to highlight the principal new dynamics.

To begin, we choose a small parameter that is some inverse power of the Stefan number and scale our dynamical equations in terms of this parameter. To motivate our choice of time scaling, we want both the heat-flux term in the Stefan condition that drives melting, and the regularizing time-derivative terms in the fluid equations to arise at this same order. Furthermore, we also require that our asymptotic analysis allows stabilizing (cubic) nonlinear terms to arise at the same order. This implies that the time-derivative terms in the fluid equations and the melting term in the Stefan condition must be second-order in our chosen expansion parameter. These conditions permit only one choice of scaling with the Stefan number. Therefore, we choose the expansion parameter $\varepsilon = S^{-1/4}$, and rescale time such that $\partial_{t^*} \to \varepsilon^2 \partial_t$, where t^* denotes the original thermal time scale from (2.1) to (2.3). The time scaling is equivalent to focusing on dynamics that depend on $t^*/S^{1/2}$, or setting the Strouhal number

$$St = S^{-1/2}. \tag{3.1}$$

Therefore

$$\frac{1}{Pr}\left(\varepsilon^2 \partial_t \boldsymbol{u} + \boldsymbol{u}\cdot\boldsymbol{\nabla}\boldsymbol{u}\right) + \boldsymbol{\nabla} P = Ra\, T\hat{\boldsymbol{z}} + \Delta \boldsymbol{u}, \tag{3.2}$$

$$\boldsymbol{\nabla}\cdot\boldsymbol{u} = 0, \tag{3.3}$$

$$\varepsilon^2 \partial_t T + \boldsymbol{u}\cdot\boldsymbol{\nabla} T = \Delta T, \tag{3.4}$$

https://doi.org/10.1017/jfm.2011.284 Published online by Cambridge University Press

$$\partial_t \eta + \varepsilon^2 \hat{\boldsymbol{n}} \cdot \boldsymbol{\nabla} T|_{z=\eta} = 0. \tag{3.5}$$

We now posit the following asymptotic expansions for our dynamical variables:

$$\boldsymbol{u} = \varepsilon \boldsymbol{u}_1 + \varepsilon^2 \boldsymbol{u}_2 + \varepsilon^3 \boldsymbol{u}_3 + O(\varepsilon^4), \tag{3.6}$$

$$T = T_0 + \varepsilon T_1 + \varepsilon^2 T_2 + \varepsilon^3 T_3 + O(\varepsilon^4), \tag{3.7}$$

$$P = P_0 + \varepsilon P_1 + \varepsilon^2 P_2 + \varepsilon^3 P_3 + O(\varepsilon^4), \tag{3.8}$$

$$\eta = \eta_0 + \varepsilon \eta_1 + \varepsilon^2 \eta_2 + \varepsilon^3 \eta_3 + O(\varepsilon^4), \tag{3.9}$$

$$Ra = R_0 + \varepsilon R_1 + \varepsilon^2 R_2 + \varepsilon^3 R_3 + O(\varepsilon^4). \tag{3.10}$$

We also employ multiple spatial scales and separate derivatives into rapidly and slowly varying components. For simplicity, we derive our envelope equations under a two-dimensional assumption, i.e.

$$\boldsymbol{\nabla} = \hat{\boldsymbol{x}} \partial_x + \hat{\boldsymbol{z}} \partial_z + \varepsilon \hat{\boldsymbol{x}} \partial_X. \tag{3.11}$$

After our equations are in place, it is simple to generalize them to higher dimensions based on standard assumptions. Also, in all of the following analysis, we find it useful to distinguish between the mean and fluctuating temperature in the following manner:

$$T(x, y, z) = \overline{T}(z) + \theta(x, y, z), \tag{3.12}$$

where the over-barred variable, $\overline{T}(z)$, is the horizontal mean of the full temperature, and $\theta(x, y, z)$ is the fluctuating temperature about this mean.

We substitute (3.6)–(3.10) into (3.2)–(3.5) and collect terms order by order. Since we must satisfy the top boundary condition for any given dynamical variable at the full value of $\eta(t, x)$, we must also expand boundary conditions order by order. Indeed, non-trivial adjustment to boundary conditions provide much of the interesting differences between our current system and traditional Rayleigh–Bénard convection.

At $O(\varepsilon^0)$, given the initial definition of the Rayleigh number, and the initial condition for the surface height,

$$\eta_0 = 1, \quad T_0 = 1 - z, \quad P_0 = R_0 \frac{T_0^2}{2}, \tag{3.13}$$

which is exactly what we obtain if we expand the solution in (2.17) using our current time scaling $t^* \to S^{1/2} t$, i.e. $St = S^{-1/2}$.

At $O(\varepsilon^1)$, since the initial conditions for the surface height are built into the initial Rayleigh number scaling we can take $\eta_1 = 0$. The mean temperature also vanishes at this order. For the fluctuating components, we define the characteristic solutions

$$w_1 = A(t, X) W_1(z) \mathrm{e}^{\mathrm{i}kx} + \text{c.c.}, \quad \theta_1 = A(t, X) \Theta_1(z) \mathrm{e}^{\mathrm{i}kx} + \text{c.c.}, \tag{3.14}$$

where $A(t, X)$ is the complex-valued envelope function determined below, and $W_1(z)$ and $\Theta_1(z)$ provide the vertical structure via

$$(k^2 - \partial_z^2) \Theta_1(z) - W_1(z) = 0, \tag{3.15}$$

$$(k^2 - \partial_z^2)^2 W_1(z) - k^2 R_0 \Theta_1(z) = 0. \tag{3.16}$$

The remaining dynamic variables take the following forms:

$$u_1 = \frac{\partial_x \partial_z w_1}{k^2}, \quad P_1 = -\frac{(k^2 - \partial_z^2) \partial_z w_1}{k^2}. \tag{3.17}$$

https://doi.org/10.1017/jfm.2011.284 Published online by Cambridge University Press

At this order, the velocity and thermal boundary conditions reduce to the standard boundary conditions for no-slip and perfectly conducting surfaces, namely

$$W_1(z=0,1)=\partial_z W_1(z=0,1)=\Theta_1(z=0,1)=0. \tag{3.18}$$

We could also make different choices for the bottom boundary conditions in (3.18). This would allow the addition of up–down symmetry-breaking terms in our eventual amplitude equations. For now, however, (3.15)–(3.18) provide the leading-order vertical structure for our system and also a characteristic leading-order Rayleigh number for any given basic wavenumber, i.e. $R_0=R_0(k)$; see figure 4.

At $O(\varepsilon^2)$, we separate the mean and fluctuating parts, and note that the mean pressure adjustment is dynamically unimportant, and the mean velocities all vanish. The $O(\varepsilon^2)$ fluctuating quantities are all identical in form to those previously computed in Schlüter, Lortz & Busse (1965) and Kuznetsov, Nepomnyashchy & Pismen (1995). The mean temperature adjustment is given by

$$\partial_z^2\overline{T}_2=\partial_z(\overline{\theta_1 w_1}), \tag{3.19}$$

with boundary conditions

$$T_2(z=0)=0, \quad T_2(z=1)+\eta_2\partial_z T_0(z=1)=0 \tag{3.20}$$

and the Stefan condition

$$\partial_t\eta_2=-\partial_z T_0|_{z=\eta_0}=1. \tag{3.21}$$

Solving (3.19)–(3.21), we obtain

$$\eta_2=t, \tag{3.22}$$

$$\overline{T}_2=tz+(1-z)\int_0^1\overline{w_1\theta_1}\,\mathrm{d}z_0-\int_z^1\overline{w_1\theta_1}\,\mathrm{d}z_0. \tag{3.23}$$

Note that (3.22) and the first term on the right-hand side of (3.23) are also consistent with (2.17), i.e.

$$\eta(t^*)=\sqrt{\frac{2t^*}{S}+1}=\sqrt{\frac{2}{S^{1/2}}\left(\frac{t^*}{S^{1/2}}\right)+1}=\sqrt{2\varepsilon^2 t+1}\approx 1+\varepsilon^2 t+O(\varepsilon^4). \tag{3.24}$$

The second and third terms in (3.23) are as expected from nonlinear convective adjustment.

The remaining $O(\varepsilon^2)$ quantities provide no differences between the traditional Rayleigh–Bénard problem and our modified Stefan system. However, at this order we do obtain a solvability condition (Hoyle 2006) in terms of the vertical eigenfunctions

$$\int_0^1(k^2W_1(z)^2+|\partial_z W_1(z)|^2)\,\mathrm{d}z=k^2R_0(k)\int_0^1\Theta_1(z)^2\,\mathrm{d}z. \tag{3.25}$$

This is the stage where the critical wavenumber is determined. The solvability condition (3.25) is only satisfied if $\partial_k R_0(k)=0$ and thus $R_0(k)$ is the minimum critical Rayleigh number and k is the critical wavenumber. For the no-slip boundary conditions currently considered, we have the standard results (Chandrasekhar 1961)

$$R_0=Ra_c\approx 1707.76, \tag{3.26}$$

$$k=k_c\approx 3.116. \tag{3.27}$$

At $O(\varepsilon^3)$ we now produce evolution equations for $A(t,X)$ and for the surface perturbations. For the third-order surface perturbations, we separate η_3 into horizontal

https://doi.org/10.1017/jfm.2011.284 Published online by Cambridge University Press

mean and fluctuating components via

$$\eta_3 = \overline{\eta}_3(t) + \Xi(t, X)\mathrm{e}^{\mathrm{i}kx} + \text{c.c.} \tag{3.28}$$

From this decomposition, we easily produce the third-order Stefan condition

$$\partial_t(\eta_3 - \overline{\eta}_3) + \partial_z\theta_1 = (\partial_t\Xi - q_1A)\mathrm{e}^{\mathrm{i}kx} + \text{c.c.} = 0, \tag{3.29}$$

where θ_1 is given by (3.14) and $\overline{\eta}_3(t)$ is the dynamically unimportant third-order mean surface perturbation.

More compactly,

$$\partial_t\Xi = q_1A \quad \text{with } q_1 = -\partial_z\Theta_1|_{z=1} \tag{3.30}$$

The thermal boundary condition at the melting surface is now given by

$$\theta_3(z=1) = \eta_3 - \overline{\eta}_3 - \eta_2\partial_z\theta_1|_{z=1} = (\Xi + q_1tA)\mathrm{e}^{\mathrm{i}kx} + \text{c.c.}, \tag{3.31}$$

which comes from interpolating from the dynamic boundary to the fixed surface $\eta_0 = 1$. The boundary condition (3.31) becomes quite important when applying the Fredholm alternative to the third-order momentum and heat equations, which requires by-parts integration, and hence knowledge of third-order boundary conditions. The fixed-temperature bottom boundary condition implies $\theta_3(z=0) = 0$.

With respect to the velocity boundary conditions, a similar interpolation to the above gives

$$w_3(z=1) = -\eta_2\partial_z w_1|_{z=1}, \quad \partial_z w_3(z=1) = -\eta_2\partial_z^2 w_1|_{z=1}. \tag{3.32}$$

Therefore, for no-slip boundaries, w_3 vanishes while $\partial_z w_3$ is non-zero.

The $O(\varepsilon^3)$ convective equations assume the following form:

$$(k^2 - \partial_z^2)\theta_3 - w_3 = -\partial_t\theta_1 - w_1\partial_z\overline{T}_2 + \ldots, \tag{3.33}$$

$$(k^2 - \partial_z^2)^2 w_3 - k^2R_0\,\theta_3 = -\frac{1}{Pr}(k^2 - \partial_z^2)\partial_t w_1 + \ldots, \tag{3.34}$$

where the '…' represent all nonlinear and modulational terms to third order that are present in the traditional non-melting Rayleigh–Bénard problem; see Schlüter *et al.* (1965) and Kuznetsov *et al.* (1995) for details.

To obtain an amplitude equation, we ensure that the right-hand sides of (3.33) and (3.34) produce no resonant forcings. Therefore, we apply a solvability condition by multiplying (3.33) and (3.34) by $\Theta_1(z)\mathrm{e}^{-\mathrm{i}kx}$ and $W_1(z)\mathrm{e}^{-\mathrm{i}kx}$ respectively, summing the two results together and integrating over $0 < z < 1$.

When performing this procedure, new non-autonomous terms appear from the by-parts integration and application of boundary conditions on the left-hand side, and the mean temperature adjustment on the right-hand side. That is, for example,

$$\int_0^1 \Theta_1\partial_z^2\theta_3\,\mathrm{d}z - \int_0^1 \partial_z^2\Theta_1\theta_3\,\mathrm{d}z = [\Theta_1\partial_z\Theta_3 - \Theta_3\partial_z\Theta_1]_0^1$$
$$= -(\Theta_3\partial_z\Theta_1)|_{z=1} = q_1(\Xi + q_1tA). \tag{3.35}$$

Therefore, after simplifying the appropriate terms, we arrive at our dynamical equation for $A(t, X)$, i.e.

$$(\mu_1t + \mu_0)A + R_0q_1\Xi = \tau_0\partial_tA + g_0\,|A|^2A - \xi_0^2\partial_X^2A, \tag{3.36}$$

where the coefficients, τ_0, μ_0, g_0, and ξ_0^2 are exactly the same as they would be if in standard Rayleigh–Bénard convection (Cross 1980; Cross & Hohenberg

https://doi.org/10.1017/jfm.2011.284 Published online by Cambridge University Press

1993). However, there are now the coefficients, μ_1, and q_1, that alter the dynamics significantly. The term $\mu_1 t$ should be expected given that, in our current regime, the Rayleigh number is increasing linearly in time. Explicitly,

$$q_1 = -\partial_z \Theta_1|_{z=1} \tag{3.37}$$

$$\mu_1 = \left[R_0 \left|\partial_z \Theta_1\right|^2 + \frac{\left|\partial_z^2 W_1\right|^2}{k^2} \right]_{z=1} - R_0 \int_0^1 W_1 \Theta_1 \, \mathrm{d}z. \tag{3.38}$$

The first group of terms in (3.38) comes from applying the boundary conditions (3.31) and (3.32) after by-parts integration in (3.33) and (3.34). The second (negative) term in (3.38) comes from the non-autonomous temperature adjustment in (3.23). Furthermore, the relative signs of these two competing terms are understandable in the sense that as the layer increases in depth, the temperature gradients (for a fixed total temperature contrast) become less adverse, but the effects of diffusion (arising from the high-order terms and hence by-parts integration) are also becoming less important, and hence less stabilizing. Thus the Rayleigh number is increasing and, as expected, $\mu_1 > 0$. Along with μ_1, there is also the $R_0 q_1 \Xi$ term in (3.36). This term additionally represents local adjustments in the relative importance of thermal diffusion due to local troughs or crests on the (now dynamic) domain height.

At this stage, it is useful to rescale our dynamical variables in both (3.30) and (3.36) according to

$$t \to \frac{\tau_0^{1/2}}{q_1 R_0^{1/2}} t - \frac{\mu_0}{\mu_1}, \quad X \to \xi_0 X, \quad A \to \frac{q_1^{1/2} \tau_0^{1/4} R_0^{1/4}}{g_0^{1/2}} A, \quad \Xi \to \frac{q_1^{1/2} \tau_0^{3/4}}{g_0^{1/2} R_0^{1/4}} \Xi, \tag{3.39}$$

which is now equivalent to

$$St = \frac{q_1 R_0^{1/2}}{\tau_0^{1/2} S^{1/2}}. \tag{3.40}$$

The rescalings (3.39) produce the much simpler form of both the convective amplitude equation and the Stefan condition,

$$\partial_t \Xi = A, \tag{3.41}$$

$$\partial_t A = \gamma t A + \Xi - |A|^2 A + \partial_X^2 A, \tag{3.42}$$

where the single new parameter is given by

$$\gamma = \frac{\mu_1}{R_0 q_1^2} \approx 3.747\,739 \tag{3.43}$$

for our chosen bottom boundary conditions. If we make the bottom thermal boundary condition flux-free (i.e. $\partial_z \Theta_1|_{z=0} = 0$), we would obtain $\gamma \approx 3.279\,187$. Importantly, this new parameter is independent of the Prandtl number, even though our amplitudes and time scalings are now dependent on Pr since τ_0 and g_0 are dependent on Pr.

4. Discussion

Ostensibly, (3.42) resembles in many ways classical Ginzburg–Landau (GL) equations (Cross & Hohenberg 1993), i.e.

$$\partial_t A = \mu A - |A|^2 A + \partial_X^2 A, \tag{4.1}$$

https://doi.org/10.1017/jfm.2011.284 Published online by Cambridge University Press

which arises in many contexts including traditional Rayleigh–Bénard convection. The GL equation (4.1) emerges in a great many situations, and is universal in the sense that its basic form can be derived from symmetry considerations alone via equivariance conditions (Hoyle 2006), and its properties are very well understood. However, in this section, we show that some of the intuition built up with respect to (4.1) does not apply to our new system (3.41) and (3.42).

If one wanted to take a minimalist approach to generalizing (4.1) to account for a dynamic transition one might think to make the simple replacement $\mu \to \gamma t$, i.e.

$$\partial_t A = \gamma t A - |A|^2 A + \partial_X^2 A \tag{4.2}$$

(e.g. Lythe 1996).

As mentioned in § 1, this could possibly model a system where the bifurcation parameter, μ, is merely a slowly varying parameter that is external to the system (such as an experimentalist slowly increasing the temperature on the boundaries of a convection experiment). With such a minimalist approach, one can show that the resulting system does indeed behave in a similar, albeit time-dependent, manner to (4.1). However, we are interested in a system where the 'bifurcation parameter' is not externally imposed, but, rather, is a slowly changing internal variable of the system. Heuristically, given the appropriate symmetries, (4.1) is the type of system one would derive when considering weakly nonlinear behaviour for systems modelled with the following general type of equations:

$$\frac{\mathrm{d}\vec{u}}{\mathrm{d}t} = \vec{F}(\vec{u};\alpha), \quad \frac{\mathrm{d}\alpha}{\mathrm{d}t} = 0, \tag{4.3}$$

where $\vec{u}$ is the set of dynamical variables (possibly infinite-dimensional), and α is the system's fixed bifurcation parameter. Furthermore, if one were to derive a system like (4.1) with the minimalist replacement $\mu \to \gamma t$, one would then start from a general system of the form

$$\frac{\mathrm{d}\vec{u}}{\mathrm{d}t} = \vec{F}(\vec{u};\alpha), \quad \frac{1}{\delta}\frac{\mathrm{d}\alpha}{\mathrm{d}t} = G(\alpha), \tag{4.4}$$

with $\delta \ll 1$ controlling the slowness of the dynamical transition. If we take $\delta \to 0$ in (4.4) we obtain $\mathrm{d}\alpha/\mathrm{d}t = 0$ and we return to (4.3). An important point to make about (4.4) is that $G(\alpha)$ does not depend on $\vec{u}$, and hence we can think of α as an external variable. Finally, though, one could consider a system of the form

$$\frac{\mathrm{d}\vec{u}}{\mathrm{d}t} = \vec{F}(\vec{u};\vec{\alpha}), \quad \frac{1}{\delta}\frac{\mathrm{d}\vec{\alpha}}{\mathrm{d}t} = \vec{G}(\vec{u};\vec{\alpha}), \tag{4.5}$$

where $\vec{G}(\vec{u};\vec{\alpha})$ now depends explicitly on the dynamic variable, $\vec{u}$, and the bifurcation parameter is now a (possibly infinite-dimensional) set of dynamical variables, $\vec{\alpha}$. As before, if we take $\delta \to 0$ we would return to (4.3). Clearly, with a redefinition of δ and a rescaling of time, (4.5) can be cast into the form of (3.2)–(3.5), with the dynamic equation for α taking the rôle of the Stefan condition, with $\delta^{-1} = S \gg 1$. Furthermore, it is not difficult to see that following the same type of procedure as in § 3, one would obtain a set of equations similar to (3.41) and (3.42) if the starting point could be cast into the form of (4.5). Benoît (1990) provides a good review of systems similar to (4.4) and (4.5) in the context of ordinary differential equations.

https://doi.org/10.1017/jfm.2011.284 Published online by Cambridge University Press

4.1. *Linear behaviour*

Examining linear dynamics is a good place to begin understanding the properties of (3.41) and (3.42). Therefore consider

$$\partial_t \Xi = A, \quad \partial_t A = \gamma t A + \Xi. \tag{4.6}$$

In the linear phase, (4.6) possesses the time-reversal symmetries $t \to -t$, $A \to \pm A$, and $\Xi \to \mp \Xi$. This symmetry is a consequence of the non-autonomous and second-order nature of (4.6), and does not apply to the standard GL equation. The minimalist extension of the GL equations (4.2) does possess the time-reflection symmetry $t \to -t$, $A \to A$ (without reference to Ξ). However, since this system is first-order in t, the solution must also be symmetric under time reflection. Therefore, a growing solution for $t > 0$ implies the dynamics must be decaying for $t < 0$. In the second-order system, there is the possibility that the solutions are not symmetric under reflection, while the equations are. That is, it is possible to have a solution that is growing for $t > 0$ and $t < 0$. This is the solution that we focus on below, but it is notable that it is anticipated from symmetry considerations.

Therefore, in the linear phase, there exist two linearly independent solutions that are the time reverses of one another. A convenient pair of linearly independent solutions is given by

$$A_\pm(t) = \int_0^\infty \zeta^{1/\gamma} \exp\left[-\frac{\zeta^2}{2\gamma} \pm \zeta t\right] \mathrm{d}\zeta, \tag{4.7}$$

$$\Xi_\pm(t) = \pm \int_0^\infty \zeta^{(1/\gamma)-1} \exp\left[-\frac{\zeta^2}{2\gamma} \pm \zeta t\right] \mathrm{d}\zeta, \tag{4.8}$$

where the $\pm$ denotes each linearly independent branch. These two solution branches are particularly convenient since one branch monotonically grows (representing convective instability), while the other monotonically decays. It is clear by inspection that (4.7) is the time derivative of (4.8); it is a little less clear that these solutions satisfy the convection equation in (4.6). However, considering the difference between the left-hand and right-hand sides, we have

$$\partial_t A_\pm - \gamma t A_\pm - \Xi_\pm = \pm \int_0^\infty (\zeta^2 \mp \gamma t \zeta - 1)\zeta^{(1/\gamma)-1} \exp\left[-\frac{\zeta^2}{2\gamma} \pm \zeta t\right] \mathrm{d}\zeta. \tag{4.9}$$

The integrand on the right-hand side of (4.9) is an exact derivative with respect to ζ, i.e.

$$(\zeta^2 \mp \gamma t \zeta - 1)\zeta^{(1/\gamma)-1} \exp\left[-\frac{\zeta^2}{2\gamma} \pm \zeta t\right] = -\gamma \frac{\partial}{\partial_\zeta}\left\{\zeta^{(1/\gamma)} \exp\left[-\frac{\zeta^2}{2\gamma} \pm \zeta t\right]\right\}, \tag{4.10}$$

where the quantity inside $\{\cdots\}$ vanishes at $\zeta = 0$ and $\zeta \to \infty$, and thus the left-hand side of (4.9) also vanishes.

With explicit formulae for linear solutions, it is also helpful to find asymptotic formulae as $t \to \pm\infty$. Also, since the two solution branches are time-reversals of each other, we simply focus on the solution that grows monotonically; see figure 3. For that solution, if we make the change of variable, $\zeta \to \zeta + \gamma t$, we obtain

$$A_+(t) \sim \sqrt{2\pi\gamma}(\gamma t)^{1/\gamma} \exp\left[\frac{\gamma t^2}{2}\right], \quad \Xi_+(t) \sim \frac{A_+(t)}{\gamma t} \quad \text{for } t \to \infty. \tag{4.11}$$

https://doi.org/10.1017/jfm.2011.284 Published online by Cambridge University Press

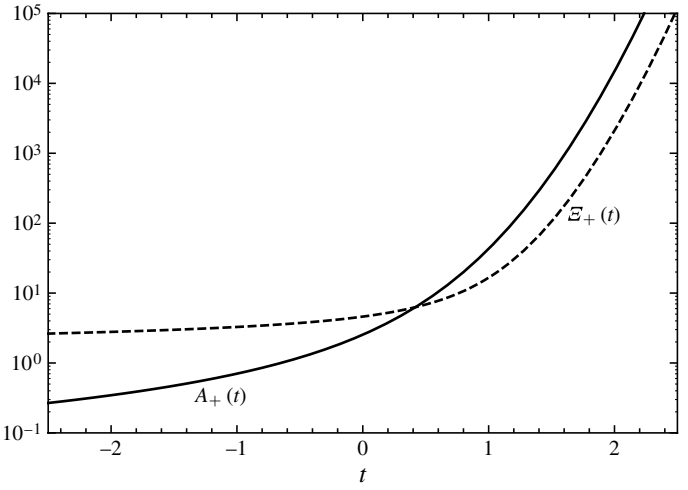


FIGURE 3. Log plots of linear eigenfunctions for the growing modes given by (4.7) and (4.8). The solid line shows $A_+(t)$. The dashed line shows $\Xi_+(t)$.

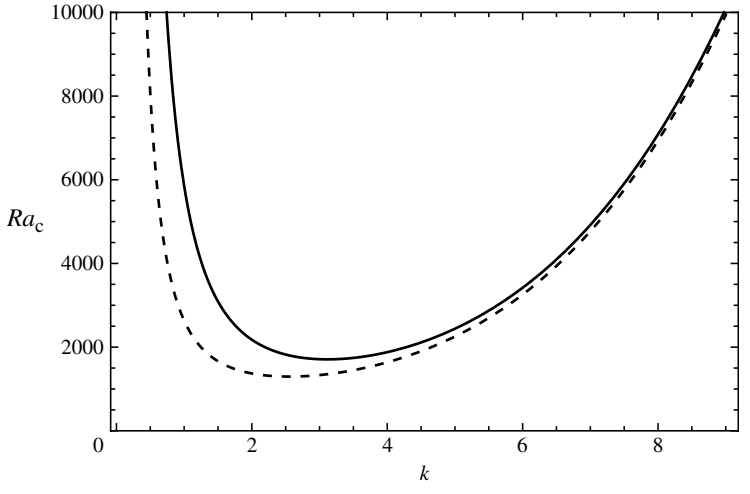


FIGURE 4. Critical Rayleigh number curves for different boundary conditions. The solid curve corresponds to perfectly conducting boundaries; the minimum occurs at $(k, Ra) \approx (3.116, 1707.76)$. The dashed curve shows marginal stability for a conducting bottom boundary and fixed-flux top boundary; the minimum occurs at $(k, Ra) \approx (2.552, 1295.78)$.

Similarly, if we make the change of variable $\zeta \to -\zeta/t$, then

$$A_+(t) \sim \frac{\Gamma\left(1+\dfrac{1}{\gamma}\right)}{|t|^{(1/\gamma)+1}}, \quad \Xi_+(t) \sim \gamma |t| A_+(t) \quad \text{for } t \to -\infty. \tag{4.12}$$

https://doi.org/10.1017/jfm.2011.284 Published online by Cambridge University Press

The linear solutions behave favourably in a number of ways. If we put back the thermal-diffusion time scale, we first observe that

$$\gamma t^2 = \frac{\mu_1}{\tau_0}\left(\frac{t^*}{S^{1/2}}\right)^2 = \left(\frac{\mu_1 t^*}{\tau_0 S}\right) t^*, \tag{4.13}$$

where t^* is the original thermal-diffusion time scale. Given that we can rescale the amplitude in (4.11) by an arbitrary factor, then

$$A_+(t^*) \sim \left(\frac{t^*}{S}\right)^{1/\gamma} \exp\left[\left(\frac{\mu_1 t^*}{2\tau_0 S}\right) t^*\right] \quad \text{for } 0 \ll t^* \ll S. \tag{4.14}$$

This shows that we can think of the amplitude growing exponentially on the time scale t^* with a growth rate and amplitude modulation that depends on the slower Stefan time scale, t^*/S. In this way, the solution (4.11) is able to capture multiple time scales with a single intermediate time scale. A single composite scale is also effective in the spatial domain for boundary layer theories (Majdalani 1998). As we should expect, the composite time scale suggests that the Stefan time scale, t^*/S, is likely interesting in its own right. This becomes more apparent when examining the past-asymptotic linear solutions. In comparison, Foster (1965) also found superexponential growth in numerical integrations of the linear phase of convection in an evaporatively cooling layer.

Since we are able to rescale the amplitude of the linear solutions by any arbitrary factor, we are also therefore able to rescale time in (4.12) by any constant factor. However, before the onset of Rayleigh–Bénard convection, the only time scale in the problem is likely to be the Stefan time, t^*/S. Therefore, the current analysis is able to capture

$$A_+(t^*) \sim \left|\frac{t^*}{S}\right|^{-((1/\gamma)+1)}, \quad \Xi_+(t^*) \sim \left|\frac{t^*}{S}\right|^{-1/\gamma} \quad \text{for } t^* \ll 0. \tag{4.15}$$

4.2. *A growing morphological mode*

As we know from (2.17) and (4.15), the presence of the Stefan number implies that t^*/S is likely an important time scale before the onset of normal convection. Therefore, we consider dynamics only on this time scale. In particular, we are interested in how small perturbations grow about the basic state defined in § 2.2. In this section, we now define $\varepsilon = S^{-1}$, and rescale time so that $\partial_{t^*} \to \varepsilon \partial_t$, which is equivalent to

$$St = S^{-1}. \tag{4.16}$$

We substitute these assumptions into (2.1)–(2.3) and (2.10), and send $\varepsilon \to 0$, and linearize about the basic state

$$\eta_0(t) = \sqrt{1+2t}, \quad T_0(z,t) = 1 - \frac{z}{\eta_0(t)}. \tag{4.17}$$

Therefore, we consider

$$\Delta \boldsymbol{u} + Ra\,\theta \hat{\boldsymbol{z}} - \boldsymbol{\nabla} P = 0, \tag{4.18}$$

$$\boldsymbol{\nabla} \cdot \boldsymbol{u} = 0, \tag{4.19}$$

$$\Delta\theta - \boldsymbol{u} \cdot \boldsymbol{\nabla} T_0 = 0, \tag{4.20}$$

$$\partial_t \eta_1 + \partial_z \theta|_{z=\eta_0(t)} = 0, \tag{4.21}$$

https://doi.org/10.1017/jfm.2011.284 Published online by Cambridge University Press

where, as before, $\boldsymbol{u}$, θ, P, and η_1 are the perturbation velocity, temperature, pressure and surface height respectively. For boundary conditions, the conditions on all the dynamical variables remain the same as before, and to reiterate, we must evaluate the top boundary condition at $z = \eta_0(t) + \eta_1(x, t)$. When expanding about $|\eta_1| \ll 1$, the linearized top boundary condition becomes

$$\theta|_{z=\eta_0(t)} + \eta_1 \partial_z T_0|_{z=\eta_0(t)} = 0. \tag{4.22}$$

The dynamics given by (4.17)–(4.22) proceeds in a different manner than in § 3. As in § 3, we Fourier-decompose and rescale all dynamic variable in the following way,

$$\eta_1 = \Xi(t)\mathrm{e}^{\mathrm{i}kx} + \text{c.c.}, \tag{4.23}$$

$$w = \Xi(t)W(z, t)\mathrm{e}^{\mathrm{i}kx} + \text{c.c.}, \tag{4.24}$$

$$\theta = \Xi(t)\Theta(z, t)\mathrm{e}^{\mathrm{i}kx} + \text{c.c.}, \tag{4.25}$$

and collapse (4.18)–(4.22) into a simplified set of amplitude equations, i.e.

$$(k^2\eta_0(t)^2 - \partial_z^2)\Theta - W = 0, \tag{4.26}$$

$$(k^2\eta_0(t)^2 - \partial_z^2)^2 W - k^2\eta_0(t)^5 Ra\,\Theta = 0, \tag{4.27}$$

where we additionally rescaled depth via $z \to \eta_0(t)z$. We also have the boundary conditions and Stefan condition for the amplitudes

$$\Theta|_{z=1} = 1, \tag{4.28}$$

$$\eta_0(t)^2\partial_t\Xi + \partial_z\Theta|_{z=1}\Xi = 0. \tag{4.29}$$

For a given instantaneous Rayleigh number, $\eta_0(t)^3 Ra$, (4.26) and (4.27) determine the amplitudes W and Θ and the wavenumber k diagnostically given the non-homogenous boundary condition (4.28) (along with the other standard boundary conditions, $W = \partial_z W = 0$ at $z = 0, 1$, and $\Theta = 0$ at $z = 0$). Given $\Theta(z)$, the Stefan condition (4.29) then determines the growth or decay of the surface-height perturbation amplitude, Ξ.

Now the following question arises: For what value of η_0 does the system begin to grow with time, rather than decay? By inspecting (4.29), we see that $\partial_t\Xi$ changes sign when $\partial_z\Theta|_{z=1} = 0$. Therefore, if solving (4.26) and (4.27) subject to a fixed-flux top boundary condition, then (4.28) simply gives a normalization condition. When this is done, we find that the critical depth and wavenumber are given by

$$\eta_0(t)^3 Ra \approx 1295.78, \tag{4.30}$$

$$\eta_0(t)k \approx 2.552. \tag{4.31}$$

This is lower than the critical depth that would be required if there were no melting-boundary dynamics (i.e. $\eta_0(t)^3 Ra \approx 1707.762$, $\eta_0(t)k \approx 3.116$); see figure 4. It is in this sense that we say that there is a 'subcritical' morphological instability, i.e. that perturbations are able to grow as a result of the deformable top boundary for an instantaneous Rayleigh number that is lower than would be required otherwise. Furthermore, figure 4 shows that the morphological instability occurs at a lower instantaneous Rayleigh number than the convective instability for all wavenumbers.

While we find finite growth for $\eta_0(t)^3 Ra \approx 1295.78$, a problem arises when the instantaneous Rayleigh number eventually passes through the critical value for traditional convection as given by (3.26). That is, the current system (4.18)–(4.22) becomes ill-posed when

$$\eta_0(t_c)^3 Ra = \eta_c^3 Ra = Ra_c \approx 1707.76. \tag{4.32}$$

https://doi.org/10.1017/jfm.2011.284 Published online by Cambridge University Press

To see how ill-posedness arises, we know that the unique solution to (4.26) and (4.27), subject to (4.32), must possess homogenous boundary conditions for both W and Θ on both boundaries. This implies that the non-homogenous condition (4.28) is inconsistent. This contradiction implies that the solutions must blow up in a finite time and our linear assumption becomes necessarily invalid. Clearly, when the system given by (4.26) and (4.27) begins to blow up, the divergence implies that there are important dynamics occurring on faster time scales, as we found in § 3.

It is instructive to see how this blowup occurs. Therefore, make the redefinition of time immediately prior to the singularity

$$\tau = \frac{3(t_c - t)}{\eta_c^2}, \tag{4.33}$$

where $t_c = (\eta_c^2 - 1)/2$ is the critical blow-up time, and consider dynamics for $0 < \tau \ll 1$. With (4.33), the instantaneous Rayleigh number is given by

$$\eta_0(t)^3 Ra = Ra_c(1 - \tau) + O(\tau^2). \tag{4.34}$$

We know that as $t \to t_c$, the unique solution to (4.26) and (4.27) must be proportional to the (traditional) critical homogenous solution, with a divergent amplitude. Therefore, we define the ansatz

$$W = \frac{W_1}{\tau} + \delta W + O(\tau), \tag{4.35}$$

$$\Theta = \frac{\Theta_1}{\tau} + \delta\Theta + O(\tau), \tag{4.36}$$

$$k = k_c, \tag{4.37}$$

where $\{W_1, \Theta_1\}$ is a non-normalized solution to the same eigenproblem as given by (3.15) and (3.16) for the critical parameters, k_c and Ra_c. The next-order amplitudes, $\{\delta W, \delta\Theta\}$, are given by the system

$$(k_c^2 - \partial_z^2)\delta\Theta - \delta W = 0, \tag{4.38}$$

$$(k_c^2 - \partial_z^2)^2 \delta W - k_c^2 Ra_c \delta\Theta = -k_c^2 Ra_c \Theta_1, \tag{4.39}$$

along with the non-homogenous boundary condition $\delta\Theta(z = 1) = 1$. Since the left-hand sides of (4.38) and (4.39) possess a null space, we apply a solvability condition by multiplying (4.38) by $k_c^2 Ra_c \Theta_1$ and (4.39) by W_1 and by integrating over z. Thus, we obtain the first term on the left-hand side of (4.39) and also a boundary contribution from the right-hand side of (4.38) following from by-parts integration. Therefore the solvability condition requires that

$$-\partial_z \Theta_1|_{z=1} = \int_0^1 W_1 \Theta_1 \, \mathrm{d}z, \tag{4.40}$$

which provides a normalization condition on the leading-order amplitudes $\{W_1, \Theta_1\}$. Recalling the definition of $q_1 = -\partial_z \Theta_1|_{z=1}$ (3.37), and given (4.40), we therefore obtain the Stefan condition

$$\partial_\tau \Xi = -\frac{q_1}{3\tau}\Xi, \tag{4.41}$$

which is written in terms of the new time variable, τ, given by (4.33). We now rescale Θ_1 to satisfy (4.40), which redefines the coefficient in (4.41) to the normalization-independent coefficient, $q_1 \to q_1^2 / \int_0^1 W_1 \Theta_1 \, \mathrm{d}z$. Therefore, recalling that we previously

https://doi.org/10.1017/jfm.2011.284 Published online by Cambridge University Press

rescaled the temperature amplitude via $\Theta \to \Xi\,\Theta/\eta_0$, (4.41) implies

$$\Theta \sim \tau^{-(p+1)}, \quad \Xi \sim \tau^{-p} \quad \text{with } p = \frac{|\partial_z \Theta_1|^2_{z=1}}{3\displaystyle\int_0^1 W_1 \Theta_1 \,\mathrm{d}z} \tag{4.42}$$

for $0 < \tau \ll 1$. However, (4.15) suggests that

$$\Theta \sim \tau^{-((1/\gamma)+1)}, \quad \Xi \sim \tau^{-1/\gamma}, \tag{4.43}$$

with γ given by (3.43). But remarkably, it can be shown that the following identity exists:

$$\gamma = \frac{3\displaystyle\int_0^1 W_1 \Theta_1 \,\mathrm{d}z}{|\partial_z \Theta_1|^2_{z=1}} \tag{4.44}$$

as a simplified version of (4.15). Moreover, (4.44) holds independently of the bottom boundary condition and implies that γ is necessarily positive.

The fact that (4.44) holds is a reassuring indication that the dynamics with time scale t/S consistently matches the dynamics with time scale $t/\sqrt{S}$. However, considering both regimes separately is important for capturing the initial growth at the first and second Ra transition when the initial time scale is insufficient to capture the onset of the traditional convective instability. The blowup at t_c is a strong indication that something is missing in the analysis with only t/S time scales and that a faster $(t/\sqrt{S})$ time scale must therefore enter the problem to regularize the divergence.

Finally, for the linear regime, it is instructive to see how the critical depth, $\eta_{0,\mathrm{c}}$, depends on the initial perturbation scale and Rayleigh number, k, Ra. That is, upon choosing relevant boundary conditions, collapsing (4.26) and (4.27) to

$$(k^2\eta_0^2 - \partial_z^2)^3 W = k^2\eta_0^5 Ra\, W \tag{4.45}$$

provides a set of values for $\eta_0 = \eta_0(k, Ra)$ where instability begins. The set of values for η_0 is given implicitly by a relation of the form

$$\eta_0^3 Ra = R_0(k\eta_0), \tag{4.46}$$

where $R_0(k)$ is a critical Rayleigh number curve for a non-melting problem with a particular set of boundary conditions, as shown in figure 4.

Figure 5 shows a set of solutions to (4.46) for both underlying curves in figure 4. The solid curves in both figures correspond to the conducting boundary conditions and hence the onset of convective instability, while the dashed curves in both figures correspond to fixed-flux boundary conditions and hence the onset of morphological instability. The particular shape of the curves in figure 5 is a reflection of the fact that as η_0 increases, not only does the instantaneous value of the Rayleigh number, $\eta_0^3 Ra$, increase, but also the critical value for a given initial wavenumber, $R_0(k\eta_0)$, varies according to figure 4. One particularly interesting feature of figure 5 is that for a given initial Rayleigh number, only a finite band of wavenumbers are ever able to begin growing. Furthermore, after a given scale becomes unstable, it only remains so for a finite period before η_0 increases sufficiently to re-stabilize the scale. This fact is made clear by the observation that (independent of boundary conditions) $R_0(k) \sim k^4$ as $k \to \infty$ and therefore there is always a sufficiently large η_0 where no solutions exist for (4.46).

https://doi.org/10.1017/jfm.2011.284 Published online by Cambridge University Press

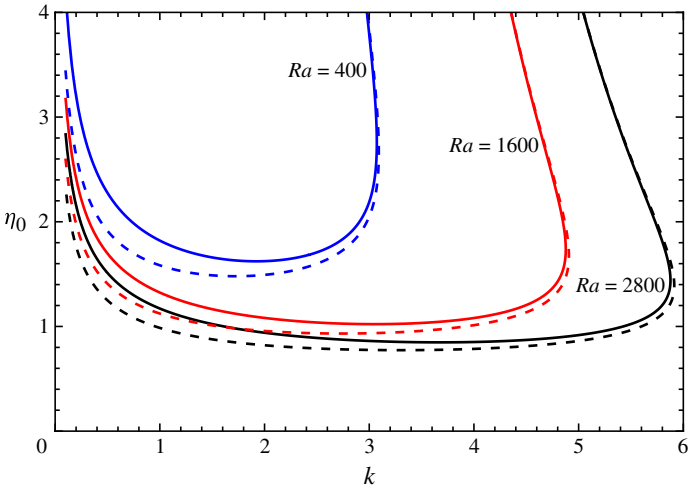


FIGURE 5. (Colour online available at journals.cambridge.org/flm) Solutions to (4.46) as a function of k for three initial Rayleigh numbers. The solid curves correspond to perfectly conducting boundary conditions (convective instability), while the dashed curves correspond to fixed-flux boundary conditions (morphological instability).

Given that any particular scale is only unstable for a finite period, we also take a cut through figure 5 to see the degree of instability as a function of η_0. Figure 6 shows the ratio of the left-hand side to the right-hand side of (4.46), alternatively the ratio of the instantaneous Rayleigh number to its instantaneous critical value for a given scale and initial value. The solid curve shows this ratio for convective instability at $(k, Ra) \approx (3.116, 1707.76)$, while the dashed line corresponds to morphological instability at $(k, Ra) \approx (2.552, 1295.78)$. It is clear that these modes only achieve a moderate degree of supercriticality before it becomes too difficult to excite these scales. However, this is not to say that the system remains moderately nonlinear. Rather, as these moderate-wavenumber modes are becoming re-stabilized, longer wavelength modes that were highly stable at early times are able to begin growing. However, because of the particular shape of figure 5, the larger scales are able to achieve a higher degree of supercriticality and remain in the nonlinear regime longer before being re-stabilized.

4.3. *Nonlinear behaviour*

Knowing that (4.6) produces superexponential growth, implying a linear instability, we are interested in the action of the nonlinear terms. Since the supercriticality (i.e., instantaneous growth rate) is linearly increasing in time, the nonlinear terms cannot saturate the instability completely. However, we do expect that the nonlinearities are at least able to arrest the superexponential growth in the instability phase. To analyse the long-time behaviour of (3.41) and (3.42), it is helpful to differentiate (3.42) with respect to time and combine the two equations into a single second-order equation for $A(t, X)$ alone, i.e.

$$\partial_t(\gamma t A - |A|^2 A) + A = (\partial_t - \partial_X^2)\partial_t A. \tag{4.47}$$

In order for the nonlinear term to balance the linearly destabilizing term, we require $|A|^2 \sim t$ as $t \to \infty$. We group all of the highest-order terms on the left-hand side of

https://doi.org/10.1017/jfm.2011.284 Published online by Cambridge University Press

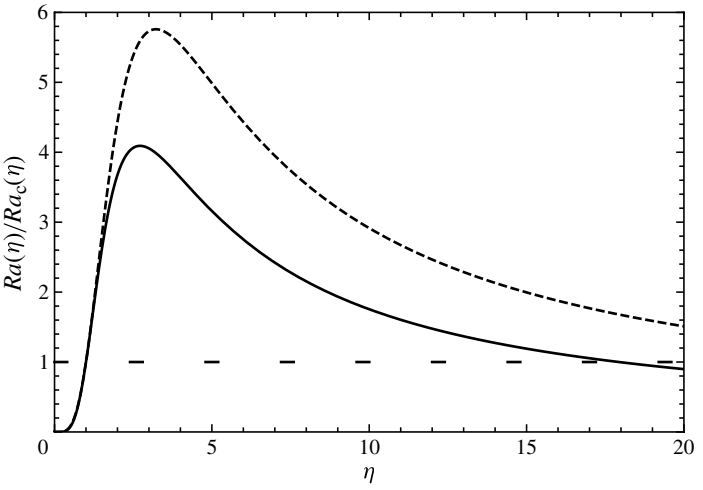


FIGURE 6. Criticality, $Ra(\eta)/Ra_c(\eta)$, versus η for convective instability at $(k, Ra) \approx (3.116, 1707.76)$ (solid) and for morphological instability at $(k, Ra) \approx (2.552, 1295.78)$ (dashed).

(4.47), and all of the lower-order terms on the right-hand side. We write the complex convective amplitude in terms of complex polar variables, and separately consider the dynamics of the real amplitude and phase (Hoyle 2006), i.e. $A(t, X) = \rho(t, X)\mathrm{e}^{\mathrm{i}\psi(t,X)}$. For the real amplitude equation

$$\rho + \partial_t(\gamma t\rho - \rho^3) = \partial_t[(\partial_t - \partial_X^2 + (\partial_X\psi)^2)\rho] - \partial_t\psi[\rho(\partial_t - \partial_X^2)\psi - 2\partial_X\rho\,\partial_X\psi], \tag{4.48}$$

where the left-hand side of (4.48) is $O(t^{1/2})$ and the right-hand side is $O(t^{-1/2})$. We find the leading-order amplitude by assuming $\rho \sim t^{1/2}$ and balancing the left-hand side of (4.48). Therefore

$$\rho(t, X) = t^{1/2}\sqrt{\tfrac{2}{3} + \gamma} + O(t^{-1/2}). \tag{4.49}$$

At this stage (4.49) is not very different from what we would obtain if we were simply considering the GL equation with a time-dependent supercriticality. In that case, $\rho = \sqrt{\gamma t} + O(t^{-1/2})$. The difference in this case is that the feedback from Ξ produces the additional $2/3$ contribution to γ.

We now clearly see from (4.49) that the cubic nonlinearity is able to arrest the superexponential growth from the linear phase. This is in contrast to the autonomous GL equation (4.1), which is able to completely saturate the instability such that $A \to \sqrt{\mu}$. That is, in the traditional GL equation, the dynamics of the system eventually become independent of the normal convective time scale, and since there are no other time scales in the problem, the dynamics becomes steady. If we now consider (4.49) with the original thermal-diffusion time scale, $t^* \sim S^{1/2}t$, we find that

$$\rho \sim \sqrt{\frac{t^*}{S^{1/2}}} \quad \text{for } t^* \to \infty. \tag{4.50}$$

However, we are really interested in the physical dynamical variables, such as the temperature perturbation, θ. But to leading order in our asymptotic expansion

https://doi.org/10.1017/jfm.2011.284 Published online by Cambridge University Press

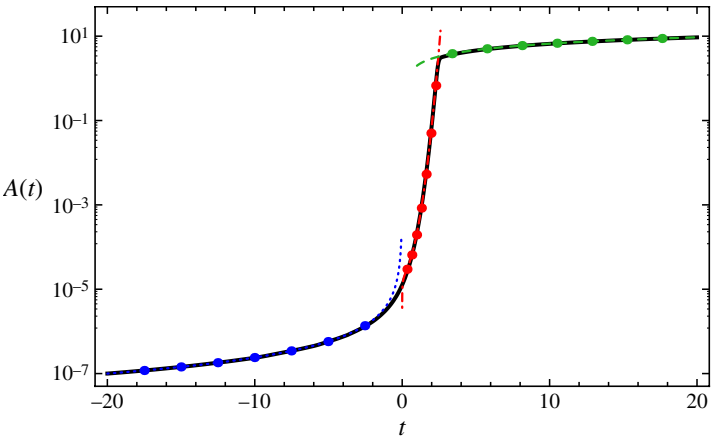


FIGURE 7. (Colour online) The solid black line shows a log–linear plot of a numerical solution to (4.47) with $\partial_X = 0$ and $\gamma = 3.747\,74$. The overlaid dotted line shows the power-law (linear) past asymptotic behaviour predicted by (4.12). The dashed line shows the superexponential (linear) future asymptotic behaviour predicted by (4.11). The dot-dashed line shows the power-law nonlinear 'saturated' dynamics as predicted by (4.49).

$\theta \sim \rho/S^{1/4}$. When combining this leading-order scaling with (4.50), the Stefan-number factors conveniently group together and we are left with

$$\theta \sim \sqrt{\frac{t^*}{S}} \quad \text{for } t^* \to \infty. \tag{4.51}$$

Likewise, the surface perturbations scale via $\Xi \sim t^{3/2}$. But the leading-order physical surface-height perturbations are scaled as $\eta(t^*) - \overline{\eta}(t^*) \sim \varepsilon^3 \Xi$, and hence

$$\eta(t^*) - \overline{\eta}(t^*) \sim \left(\frac{t^*}{S}\right)^{3/2} \quad \text{for } t^* \to \infty. \tag{4.52}$$

That is, the long-time behaviour of our physical quantities only depend on the Stefan time scale, t^*/S, and not the convective time scale, t^*, nor the intermediate time scale, $t^*/S^{1/2}$. Furthermore, we see clearly that our asymptotic expansion remains valid for roughly a Stefan time, i.e. $t^* \sim S$. However, the system is able to fall into the long-time scaling regime after only a time of roughly $t^* > S^{1/2}$ (or less). Therefore, if the Stefan number is large enough so that there is reasonable separation between $1 \ll S^{1/2} \ll S$, then we expect to see the clear transition between slow algebraic growth for $t < 0$, to superexponential growth for somewhat-large $t > 0$, and back to slow algebraic growth for t larger than that. Figure 7, which shows the numerical solution of the system, bears out this expectation.

Eventually, after a full Stefan time, the layer depth, and hence also the Rayleigh number, changes by order unity After this time, we would be away from the weakly nonlinear regime and into a more strongly nonlinear regime. Interestingly, though, given the phase dynamics we examine below, the weakly nonlinear dynamics of our system may strongly influence the later structure of the solutions.

In a similar manner to (4.48), we produce an equation for phase dynamics

$$\begin{aligned}(\gamma t\rho - \rho^3)\partial_t\psi = {} & \partial_t[\rho(\partial_t - \partial_X^2)\psi - 2\partial_X\rho\,\partial_X\psi] \\ & + \partial_t\psi(\partial_t - \partial_X^2 + (\partial_X\psi)^2)\rho,\end{aligned} \tag{4.53}$$

https://doi.org/10.1017/jfm.2011.284 Published online by Cambridge University Press

where the right-hand side of (4.53) is $O(t^{-1/2})$. Given (4.49), we find that

$$\partial_t \psi(t, X) = O(t^{-2}), \tag{4.54}$$

which implies that, to leading order,

$$\psi(t, X) = \psi_0(X) + O(t^{-1}), \tag{4.55}$$

where at this stage, $\psi_0(X)$ is a completely arbitrary function of the spatial variable, X. Furthermore, we can determine all of the higher-order terms in (4.49) and (4.55) in terms of $\psi_0(X)$, e.g. given (4.49), we find that

$$\rho(t, X) = t^{1/2}\sqrt{\frac{2}{3} + \gamma}\left(1 - \frac{[\partial_X \psi_0(X)]^2}{2\gamma t} + O(t^{-2})\right), \tag{4.56}$$

$$\psi(t, X) = \psi_0(X) - \frac{3}{4}\frac{\partial_X^2 \psi_0(X)}{t} + O(t^{-2}). \tag{4.57}$$

The long-time behaviour given by (4.55) is one of the most surprising new features of (4.47). That is, for long times, the solution grows algebraically in time, but with a 'locked-in' spatial pattern that may be very complicated. These patterns are determined by the initial conditions.

The 'locked-in' behaviour derived from (4.57) is not so much a consequence of the non-autonomous nature of (3.42), but rather of the presence of the feedback from the Stefan condition (3.41), i.e. the second-order nature of the system as a whole. In (4.47), a time derivative on the left-hand side exists because we must differentiate the amplitude equation to eliminate the surface-height perturbations, $\Xi(t, X)$. By contrast, in the GL equation, there are no derivatives acting on the leading-order terms, and therefore the phase cannot enter until a higher order. In this situation, the phase dynamics are simply diffusive, which produces $\partial_X^2 \psi \sim O(t^{-1})$, or $\psi(X)$ is simply a linear function of X for long times.

At this stage, we know that our system contains the potential to produce self-similarly growing locked-in patterns, but the only thing that we know about how the patterns are selected is that they are determined some time during the transient relaxation to the self-similar state. Furthermore, we have no information as to what the patterns actually look like. We can presume that not all possible locked-in patterns, $\psi_0(X)$, are equally stable. For the time being, the best method to obtain insight into the structure of $\psi_0(X)$ is through numerical simulation.

5. Numerical analysis

In this section we present some of the numerical solutions of our system (3.41) and (3.42) and some of its simplifications and generalizations.

5.1. *Real-amplitude dynamics*

First, we highlight the different amplitude-scaling regimes that are discussed in § 4. Figure 7 shows the numerically integrated solution to the following (real) ordinary differential system with no spatial modulation:

$$\partial_t \Xi = A, \quad \partial_t A = \gamma t A + \Xi - A^3. \tag{5.1}$$

We integrate forward in time from $t = -20$ subject to the initial conditions, $A(t = -20) = 10^{-7}$, and $\Xi(t = -20) = 20\gamma \times 10^{-7}$, where the condition for Ξ is chosen to select the monotonically growing linear solutions given by (4.12). In

https://doi.org/10.1017/jfm.2011.284 Published online by Cambridge University Press

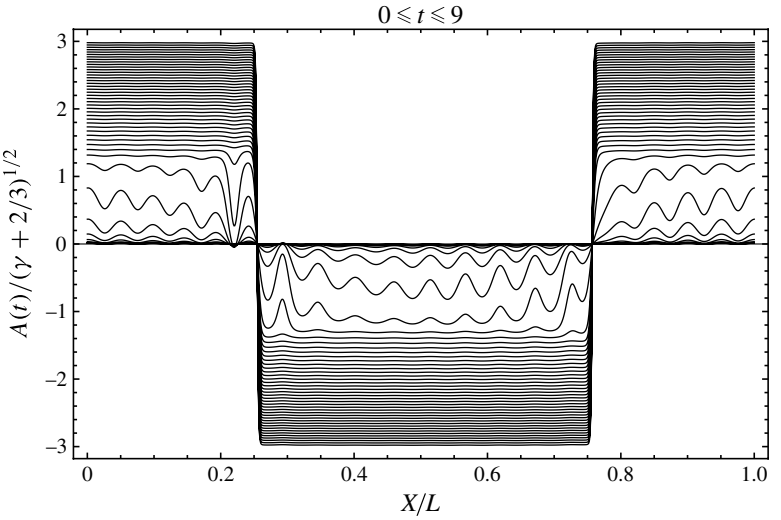


FIGURE 8. A series of plots showing the time evolution of a steepening real pattern. The pattern begins with small-amplitude initial perturbations, and eventually settles into two fronts with amplitude growing according to $t^{1/2}\sqrt{\gamma + 2/3}$.

figure 7, we clearly see the three separate time-growth regimes given by (4.11), (4.12), and (4.49), where the transition between each regime is separated by a rather brief period of more complex dynamics. For the first transitions (near $t \approx 0$), the dynamics are very well approximated by the full form of (4.7), whereas the transition to nonlinear behaviour is not well described analytically.

Also, as an intermediate step between the system with no spatial modulation and the one with complex phase dynamics, we also consider a purely real system with spatial modulation:

$$\partial_t \Xi = A, \quad \partial_t A = \gamma t A + \Xi - A^3 + \partial_X^2 A. \tag{5.2}$$

This system given by (5.2) is interesting because it demonstrates growing 'front' solutions that join regions where $A \approx \pm t^{1/2}\sqrt{\gamma + 2/3}$. This type of behaviour is shown in figure 8 for similar parameters as considered in the complex-amplitude cases considered below. These types of solutions are very similar to those obtained from considering the intermediate dynamic Ginzburg–Landau system given by (4.2).

5.2. *Complex-amplitude dynamics*

This section's goal is to gain some understanding of phase dynamics in the presence of spatial modulation. Therefore, we discuss solutions to the (complex) partial differential system given by (3.41) and (3.42) in a large periodic domain, $0 \leqslant X \leqslant L$. In our calculations, we fix $L = 40\pi$. In order to study the distribution of possible frozen-in phase functions we initiate a series of integrations with random starting conditions of the form

$$A(t=0) = \sum_{|k| \leqslant K} \hat{\alpha}_k \mathrm{e}^{\mathrm{i}2\pi k X/L}, \quad \Xi(t=0) = \sum_{|k| \leqslant K} \hat{\xi}_k \mathrm{e}^{\mathrm{i}2\pi k X/L}, \tag{5.3}$$

where $\hat{\alpha}_k, \hat{\xi}_k$ are independent, identically distributed, complex Gaussian random variables and with zero mean and standard deviation $A_0(2K+1)^{1/2}$. We choose

https://doi.org/10.1017/jfm.2011.284 Published online by Cambridge University Press

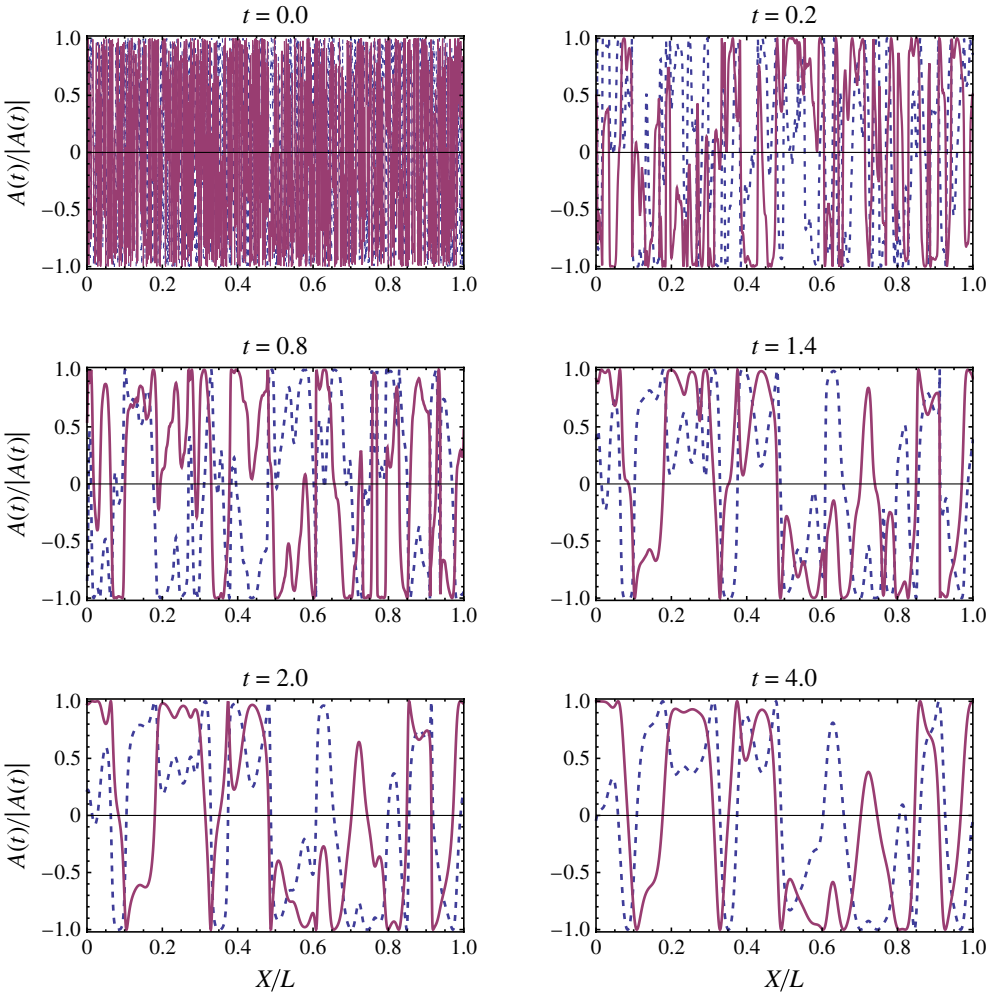


FIGURE 9. (Colour online) A series of plots showing the time evolution of complex pattern $A(t, X)/|A(t, X)|$ The real component is shown in blue (dashed) and the imaginary component is shown in mauve (solid). After $t \approx 4.0$ the pattern does not evolve any further.

$K = 512$ and $A_0 = 10^{-3}$. Note that the expectation of the norms of our dynamical variables are given by

$$\left\langle \frac{1}{L} \int_0^L |A(X)|^2 \, \mathrm{d}X \right\rangle = \sum_{|k| \leqslant K} \langle |\hat{\alpha}_k|^2 \rangle = A_0^2. \tag{5.4}$$

The initial statistics of Ξ are identical to those of A.

We solve (5.2) pseudospectrally, whereby cubic/quadratic multiplications are computed in a grid space and derivatives are computed in wavenumber space. We transform between the two spaces with a fast Fourier transform. Given that we are working with a cubic nonlinearity, we must dealias our transforms by a factor of two, i.e. we must use twice as many grid points as spectral modes to keep our results free from aliasing errors. For the timestepping scheme, we use a second-order Runge–Kutta exponential-time-differencing scheme. That is, we

https://doi.org/10.1017/jfm.2011.284 Published online by Cambridge University Press

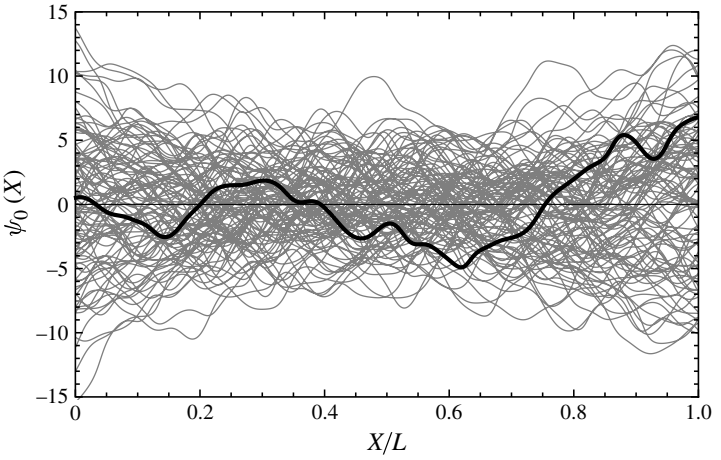


FIGURE 10. A collection of steady phase functions, $\psi_0(X)$, in grey to show the variance for 100 different random initial conditions. The black line highlights the realization shown in figure 9.

employ exponential-time-differencing for the (stiff) diffusion terms combined with a second-order Runge–Kutta method for the remaining linear and nonlinear terms (see the ETD2RK method of Cox & Matthews 2002). As mentioned above, the computations are initiated with random white noise and allowed to evolve until a fixed pattern is achieved. In one dimension, it is relatively easy to achieve high-resolution computations, hence we use 2048 grid points, equivalent to 1024 spectral modes (with initial power up to 512 spectral modes).

Even for the complex-amplitude dynamics, figures 7 and 8 both give a good picture of how the real modulus, $|A(t, X)|$, evolves as a function of time. While figure 7 contains no spatial information, we see from (4.56) that the spatial inhomogeneities of $|A(t, X)|$ decay as $\sim t^{-1}$ in a form that depends on the spatial form of the phase function. Therefore, at this stage, we are most interested in the dynamics of the normalized amplitude

$$\frac{A(t, X)}{|A(t, X)|} = \mathrm{e}^{\mathrm{i}\psi(t,X)}. \tag{5.5}$$

Figure 9 shows the time evolution of $\mathrm{Re}[A/|A|] = \cos\psi$ and $\mathrm{Im}[A/|A|] = \sin\psi$ where Re and Im are the real and imaginary parts, respectively. In each frame the blue line shows $\cos\psi(t, X)$ and red line shows $\sin\psi(t, X)$ as a function of X. After $t = 0$, the initial dynamics are marked by the rapid decay of the high-wavenumber components of the initial Gaussian white noise. Eventually the pattern settles into a locked state consisting of mostly large scales.

Figure 10 shows directly the final locked phase function for an ensemble of initial data. The solid black line shows the particular realization shown in the final frame of figure 9. The collection of grey lines show the variance over 100 (out of 600 total) realizations. Regardless of the initial distribution (uniform or Gaussian), the final spatial fluctuations of $\psi_0(X)$ are Gaussian-distributed.

Figure 11(*a*) shows the spatial power spectrum of the phase function after subtracting out a linear background, i.e. the power spectrum of $\psi_0(X) - \psi_0(0) - X\psi_0(L)/L$. The solid black line shows the geometric average over 600 realizations,

https://doi.org/10.1017/jfm.2011.284 Published online by Cambridge University Press

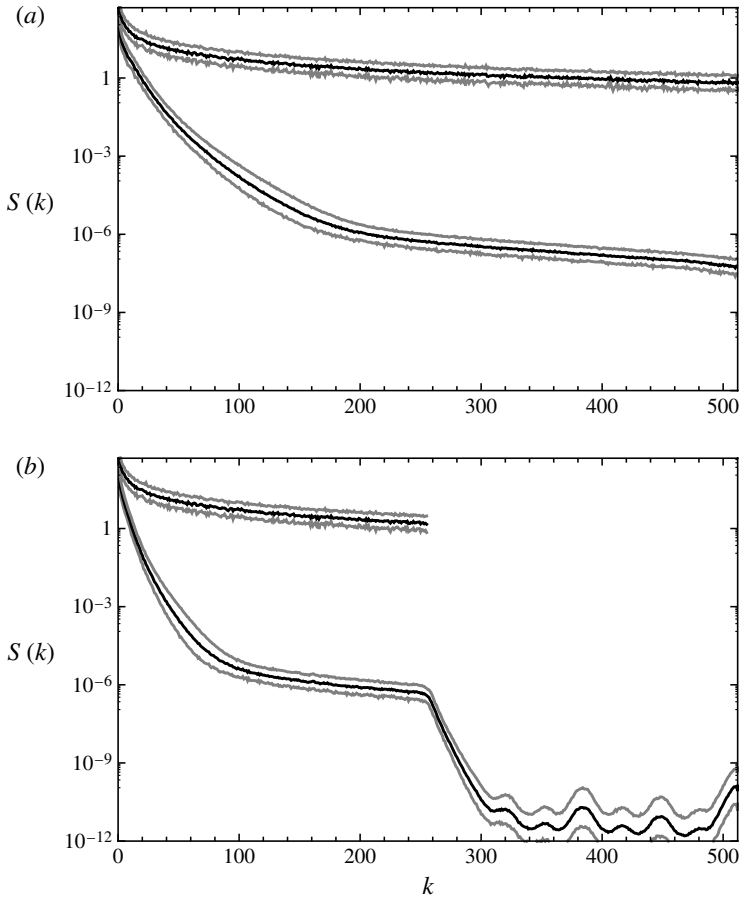


FIGURE 11. Ensemble-averaged spectrum of the locked-in phase function, $\psi_0(X) - \psi_0(0) - X\psi_0(L)/L$, given by (4.55). In each case, the top set of lines gives the initial spectrum, the bottom set gives the spectrum of the locked-in pattern. The middle black lines give the geometric mean of the phase spectrum averaged over 600 realizations of (5.2). The grey lines give the standard deviation about the mean. The initial spectrum is close to a power law with scaling exponent ≈ -1. Both sets of calculations are computed at a resolution of 512 dealiased wavenumbers (1024 total modes, 2048 grid points). Panels (*a*) and (*b*) show the results for two different initial spectra.

and the grey lines show the variance over the ensemble. The top set of lines gives the average initial spectrum given by (5.3), and the bottom set the final spectrum. After the dynamics runs its course, the power in the small scales declines dramatically. Interestingly, the final spectrum takes the form of two (approximately) power-law spectra with different exponents. The location of the bend scaling law appears to coincide roughly with the midpoint in the initial spectrum. However, this location is not related to the resolution of the computation. Indeed, when running a set of computations with the same resolution, but only half the initial bandwidth (figure 11*b*), the bend in the final power law shifted to the corresponding location. The reasons for this feature are not entirely clear. However, it seems reasonable that as the initial bandwidth increases, the location of the elbow is pushed to a higher wavenumber and the dominant scaling is the steeper of the two branches.

https://doi.org/10.1017/jfm.2011.284 Published online by Cambridge University Press

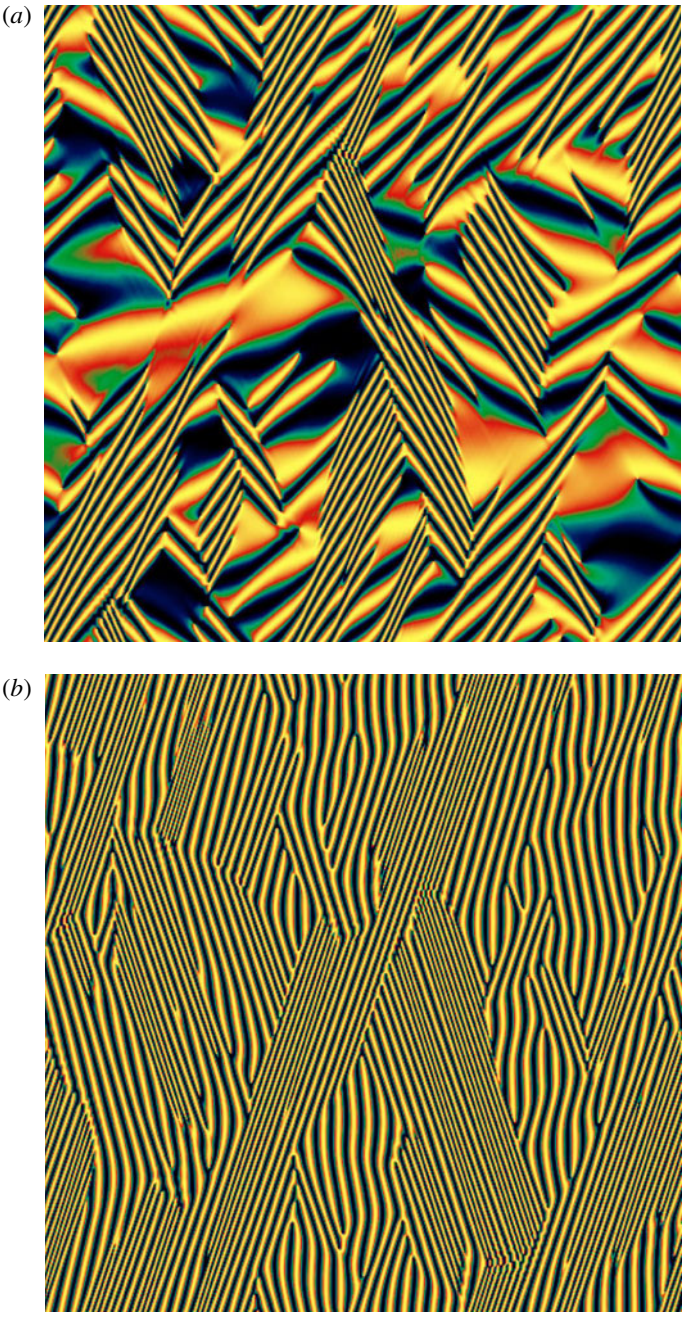


FIGURE 12. (Colour online) A solution showing a steady 'locked-in' pattern. (*a*) The locked-in pattern solution to (5.6), i.e. $\cos[\psi_0(X, Y)]$. (*b*) A corresponding example on the same domain with an underlying small-scale carrier wave, i.e. $\cos[\psi_0(X, Y) + 100X]$.

5.3. *Two-dimensional patterns*

5.3.1. *Rolls*

The simplest extension of our model into an additional dimension is to assume an underlying one-dimensional pattern with two-dimensional modulations (Newell &

https://doi.org/10.1017/jfm.2011.284 Published online by Cambridge University Press

Whitehead 1969; Segel 1969). If we still assume that the underlying (rapidly varying) pattern is one-dimensional, then we would use an anisotropic modulation and simply make the replacement $\partial_X \to \partial_X + \mathrm{i}\partial_Y^2$, i.e.

$$\partial_t \Xi = A, \quad \partial_t A = \gamma t A + \Xi - |A|^2 A + (\partial_X + \mathrm{i}\partial_Y^2)^2 A. \tag{5.6}$$

Figure 12(*a*) shows the real part of a direct solution to (5.6) with low-amplitude Gaussian white noise initial conditions. The box size is $40\pi \times 40\pi$, and the spatial resolution is 768 collocation points in each direction. Since the modulus of the solution, $|A|$, is mostly spatially uniform at late times, figure 12(*a*) shows primarily

$$\mathrm{Re}[A(X, Y)] \approx \cos[\psi_0(X, Y)], \tag{5.7}$$

where $\psi_0(X, Y)$ is the two-dimensional version of the locked-in phase function from (4.55).

It is interesting that the pattern is marked by regions of rapid modulation directly adjacent to relatively large regions of much smoother behaviour. The clear presence of defects is also a notable feature of the small-scale modulation regions. Figure 12(*b*) shows the same modulational pattern as in figure 12(*a*), along with a small-scale carrier pattern. That is, we show an example of a 'physical' amplitude via

$$\theta \sim A(X, Y)\mathrm{e}^{\mathrm{i}X/\varepsilon} + \text{c.c.}, \tag{5.8}$$

with $\varepsilon = 1/100$. In this case one can see how the varying regions in the complex amplitude, A, correspond to moderate local dilatations and contractions of the scale of the underlying carrier wave. In comparison to (5.7), figure 12(*b*) shows

$$\theta \sim \cos[\psi_0(X, Y) + 100X]. \tag{5.9}$$

We also see quite abrupt 'zigzags' in the reconstructed pattern. We speculate that these features are produced from a dynamic form of modulational instabilities (Eckhaus and zigzag) that get frozen in at different stages of their evolution at different locations in the domain (Hoyle 2006). However, more study is clearly needed to understand the detailed reasons behind why particular patterns are chosen over others.

5.3.2. *Hexagons*

Normally, if we consider traditional patterns that cannot lock in, then given the presence of up–down symmetry specifically in Rayleigh–Bénard convection, the preferred underlying pattern would indeed be one-dimensional rolls. However, since the current system is capable of locking in a complex pattern, we should anticipate the presence of locally broken up–down symmetry, even if the basic equations are symmetric at the order we are considering, and do not possess stable hexagonal solutions. This is another key difference between our new system and the classical GL equation, where, for the parameters of Rayleigh–Bénard convection, the latter only prefers a hexagonal pattern in the presence of explicit symmetry-breaking terms, such as weak non-Boussinesq effects (Schlüter *et al.* 1965; Busse 1967; Hoyle 2006).

Therefore, we can generalize (3.41) and (3.42) to model an instability about a system of three independent rolls that are rotated at an angle of 120° with respect to one another. This allows for hexagonal patterns and also local roll or square patterns, or some more complicated mixture. This requires a separate convective amplitude and surface-height perturbation for each set of separate rolls, i.e. A_i, and Ξ_i, where $i = 1, 2, 3$. Also, for completeness, we can include terms that explicitly break up–down symmetry, both from weak (i.e. $O(\varepsilon)$) non-Boussinesq effects (Hoyle 2006) and also from effects such as non-symmetric top and bottom boundary conditions (Kuznetsov

https://doi.org/10.1017/jfm.2011.284 Published online by Cambridge University Press

et al. 1995). The most reasonable choice that we could make in this respect would be to pose the full equations with a fixed-heat-flux bottom boundary condition, rather than the assumed fixed-temperature condition. When making the above generalizations,

$$\partial_t \Xi_1 = A_1, \tag{5.10}$$

$$\partial_t A_1 = \gamma t A_1 + \Xi_1 - |A_1|^2 A_1 - g_1(|A_2|^2 + |A_3|^2)A_1 + \chi A_2^* A_3^* + \mathrm{i}h_1(A_3^* \partial_{X_2} A_2^* + 2A_2^* \partial_{X_2} A_3^* + A_2^* \partial_{X_3} A_3^* + 2A_3^* \partial_{X_3} A_2^*) + \partial_{X_1}^2 A_1, \tag{5.11}$$

$$\partial_t \Xi_2 = A_2, \tag{5.12}$$

$$\partial_t A_2 = \gamma t A_2 + \Xi_2 - |A_2|^2 A_2 - g_1(|A_1|^2 + |A_3|^2)A_2 + \chi A_1^* A_3^* + \mathrm{i}h_1(A_3^* \partial_{X_1} A_1^* + 2A_1^* \partial_{X_1} A_3^* + 2A_1^* \partial_{X_3} A_3^* + A_3^* \partial_{X_3} A_1^*) + \partial_{X_2}^2 A_2, \tag{5.13}$$

$$\partial_t \Xi_3 = A_3, \tag{5.14}$$

$$\partial_t A_3 = \gamma t A_3 + \Xi_3 - |A_3|^2 A_3 - g_1(|A_1|^2 + |A_2|^2)A_3 + \chi A_1^* A_2^* + \mathrm{i}h_1(A_2^* \partial_{X_1} A_1^* + 2A_1^* \partial_{X_1} A_2^* + A_1^* \partial_{X_2} A_2^* + 2A_2^* \partial_{X_2} A_1^*) + \partial_{X_3}^2 A_3, \tag{5.15}$$

where $\hat{\boldsymbol{k}}_1 = (1, 0)$, $\hat{\boldsymbol{k}}_3 = (-1/2, \sqrt{3}/2)$, $\hat{\boldsymbol{k}}_2 = (-1/2, -\sqrt{3}/2)$ now give the three unit wavevectors for the basic patterns of rolls, and $\partial_{X_i} = \hat{\boldsymbol{k}}_i \cdot (\partial_X, \partial_Y)$ gives the modulational derivatives in those directions. In (5.10)–(5.15), g_1 gives the nonlinear cross-coupling between the basic individual rolls, h_1 is an $O(1)$ symmetry-breaking coefficient owing to advection effects under the Boussinesq framework (such as symmetry breaking via boundary conditions), and χ is a symmetry-breaking coefficient owing to $O(\varepsilon)$ non-Boussinesq effects (Hoyle 2006). We note that the terms multiplying the h_1 coefficient are in their particular form to ensure that advection does not contribute to the overall energy balance.

The system given by (5.10)–(5.15) possesses stable hexagonal solutions for $1 > g_1$ (Golubitsky, Swift & Knobloch 1984). However, this is not the situation for our current Rayleigh–Bénard convection problem where $g_1 \approx 1.4$. Regarding non-Boussinesq effects, we note that χ cannot contain any contributions either from the small non-uniformity of the basic temperature gradient or from any effect of the melting interface deformation. Such effects are all $O(S^{-1}) = \varepsilon^4$ less than the terms that we include in our asymptotic analysis. These effects are far too weak to contribute quadratic terms to (5.10) and (5.11). Therefore, the only quadratic terms result from effects that would traditionally produce quadratic nonlinearities (such as a slight temperature-dependent viscosity/thermal conductivity and/or coefficient of thermal expansion), and modulational effects are limited in the ways that we discussed above.

If should be noted that in the steady-state analysis of Davis *et al.* (1984) the coefficient equivalent to χ is not small. This is because there is no Stefan number dependence in the steady state. In our problem, the evolution of the convection occurs on a much faster time scale than the evolution of the mean interface. Therefore, the interface deformations are much smaller than are possible in the steady case.

In the particular case ($h_1 = \chi = 0$) considered here, (5.10)–(5.15) possesses strict up–down symmetry, although the solutions do necessarily not share this feature. In the dynamic problem, if $|g_1| < 1$, the system is able to lock in arbitrary phase relationships between (A_1, A_2, A_3), and the amplitudes all tend to the same value, leading to complicated patterns. If $|g_1| > 1$, locally one of the three amplitudes dominates, with an arbitrary spatially dependent phase function, leading to patches of distorted rolls separated by defects and grain boundaries.

https://doi.org/10.1017/jfm.2011.284 Published online by Cambridge University Press

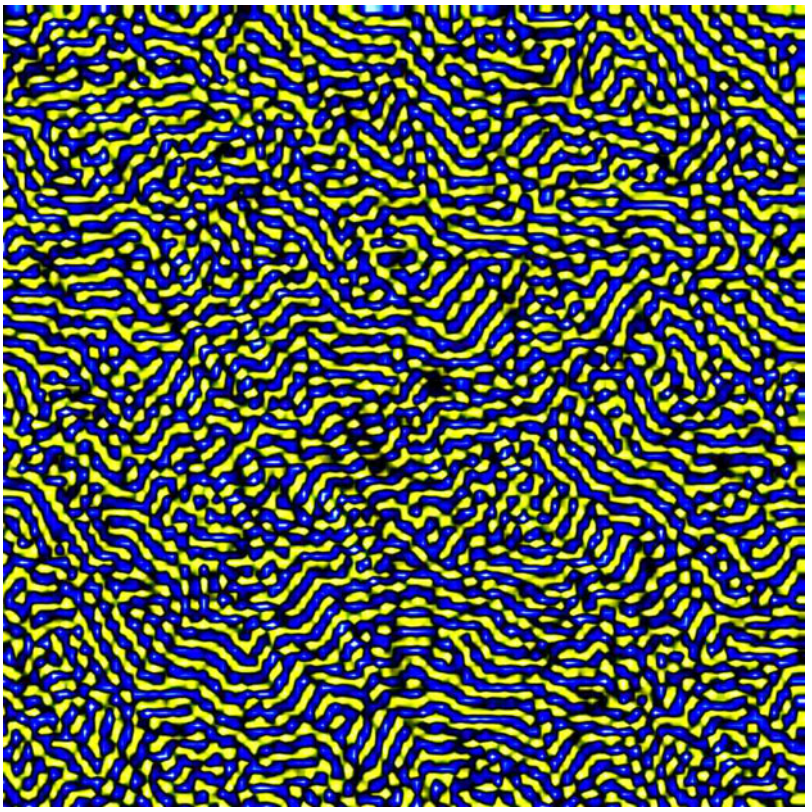


FIGURE 13. (Colour online) A solution to (5.10)–(5.15) with $g_1 = 1.415\,32$, $h_1 = \chi = 0$, and $\gamma = 3.747\,74$ showing a steady 'locked-in' pattern given by (5.16) with $\varepsilon = 1/100$. Blue tones represent negative values and yellow tones represent positive values, with black representing neutral values.

It is interesting to consider solutions with parameter values, and in particular, boundary conditions that we used to derive the system in § 3, i.e. no explicit symmetry-breaking terms from boundary conditions. Taking the limit of infinitely large Prandtl number and fixed-temperature top and bottom boundary conditions, one obtains values of $g_1 = 1.415\,32$, $h_1 = 0$ and $\gamma = 3.747\,74$. If we assume there are no non-Boussinesq effects, then $\chi = 0$ and (5.10)–(5.15) possesses reflection symmetry.

Recalling again that the spatial variation of the amplitudes, $A_i(X_1, X_2, X_3)$, is a modulation about a background consisting of three independent roll patterns, the physical pattern, for say the temperature perturbations, is given by

$$\theta \sim A_1 \mathrm{e}^{\mathrm{i}kx_1} + A_2 \mathrm{e}^{\mathrm{i}kx_2} + A_3 \mathrm{e}^{\mathrm{i}kx_3} + \text{c.c.}, \tag{5.16}$$

where $x_i = X_i/\varepsilon$ for some unspecified $\varepsilon \ll 1$.

Figure 13 shows the steady locked-in pattern that results from a calculation with the above parameters with $\varepsilon = 1/100$. In this case, we still use reasonably large box dimensions of $20\pi \times 20\pi$ and 512 collocation points in each direction. It is clear that, locally, the pattern is primarily roll-like, but that the direction of rolls changes from region to region and that the pattern occasionally assumes a more cellular nature in a number of patches. Interestingly, there even appear to exist a few isolated locations within the domain where the convection comes very close to shutting itself off on

https://doi.org/10.1017/jfm.2011.284 Published online by Cambridge University Press

scales that are somewhat larger than the typical stagnation regions between up-flow and down-flow regions.

6. Conclusions

We derive a new class of envelope equations for dynamics near a time-dependent bifurcation. We believe that these equations are likely to be valuable in modelling both the current configuration, and perhaps a variety of other systems. The greatest difference between our current system and other equations used to model dynamic transitions (Lythe 1996) is the presence of the feedback onto the surface-height perturbations. That is, we model dynamic transitions where the bifurcation 'parameter' is actually a slowly changing variable of the system, as opposed to an externally determined parameter.

It is instructive to recount the sequence of events that one could expect to see in an actual setup of our system. Specifically, we could expect a number of distinct phases in the dynamics. That is: (i) if the system is initiated with a sufficiently low Rayleigh number, then perturbations are damped and one would only observe the growth of the uniform layer depth on a Stefan time scale; (ii) eventually the instantaneous Rayleigh number would become sufficient for the growth of perturbations initially evolving on a Stefan time scale, but with growth rate continually increasing; (iii) when the Rayleigh number becomes close to the traditional critical value for an equivalent non-melting system, one would see a rapid increase in the amplitude as the system undergoes superexponential growth and a rapid pattern readjustment; (iv) eventually the superexponential growth is arrested in a weakly nonlinear regime and one would see the system saturate to slow power-law growth, again on a Stefan time scale, along with a complex locked-in spatially inhomogeneous pattern; (v) finally, after roughly a full Stefan time, the system would move into a strongly nonlinear regime and more complex spatial and temporal behaviour would likely result.

There are also a number of alternative physical systems that contain an internal bifurcation parameter. Obvious examples of systems likely to display similar dynamics are other Stefan systems that include a variety of other dynamical ingredients, some of which we mention below. Furthermore, deagration/detonation (i.e. combustion) systems under the action of buoyancy could also provide another class of systems exhibiting many of the dynamical pattern-forming behaviours outlined in the current work (Landau & Lifshitz 1995). Specifically, one could envisage an increasingly accelerating burning front succumbing to buoyancy instabilities once a critical acceleration rate is achieved. Local mixing would then provide the feedback needed to cast the system into the general form discussed in § 4.

In many other systems, it could be possible to produce scaled equations where the coefficients are complex, as opposed to purely real. That is, it is expected that there are extensions to (3.41), (3.42) that more resemble a Ginzburg–Landau equation with complex coefficients (Cross & Hohenberg 1993). Possible systems that may contain richer dynamics than the current melting-boundary problem include other Stefan problems where one or more boundaries are not only able to melt, but can also dissolve. Woods (1992) considered the general framework for melting–dissolving problems, which are also considered experimentally by Liu, Ning & Ecke (1996) and Sullivan, Liu & Ecke (1996). Qualitatively, the results from these experimental works, along with those by Davis *et al.* (1984) in melting-wax systems, are reasonably consistent with our numerical calculations. In particular, melting–dissolving systems should be interesting given that the two-component dynamics would allow for various

https://doi.org/10.1017/jfm.2011.284 Published online by Cambridge University Press

double-diffusive behaviours, which, among others, include Hopf bifurcations at leading order. The presence of a complex fundamental growth rate would lead to a complex dynamic Ginzburg–Landau-type equation, which could produce interesting nonlinear oscillations, or even chaotic behaviour. We intend to investigate these possibilities in future work.

Finally, it is intriguing to consider the experimental possibilities that would be relevant to our current system and its asymptotic approximations. There are a number of substances that possess a large enough latent heat to provide a large Stefan number for reasonable temperature differences. For water, $L_{fusion}/c_p \approx 80$ K. Therefore, a temperature contrast of $T_b - T_m \approx 1$ K would provide a large enough separation between $S \approx 80$ and $S^{1/2} \approx 9$ for our above analysis to remain reasonable. Of course, water complicates issues because of its density maximum at $T \approx 4\,^{\circ}$C. To avoid this issue, one could simply use another substance, e.g. wax as in Davis *et al.* (1984). Or, for $T_b - T_m \leqslant 4$ K, our system could be easily produced with water/ice if the bottom boundary was made of ice and allowed to melt. Furthermore, it would also be an interesting theoretical extension to our current work to consider the dynamics of a water/ice system, where we would expect penetrative convection into a region below the melting solid interface (Moore & Weiss 1973). In this case, we could still reasonably expect $S \approx 10$–20. We intend to address this environmentally interesting case in future work.

This research was conducted while G.M.V. was a visiting scholar at DAMTP at the University of Cambridge through generous support from Trinity College. Both G.M.V. and M.R.E.P. would like thank J. H. P. Dawes, M. G. Worster, J. Wettlaufer and N. H. Brummell for valuable comments and discussions. This research was also supported by NASA Solar and Heliospheric Division Supporting Research and Technology grant no. NNG04GB86G and NASA Sun–Earth Connection Theory Program grant no. NNG05G124G.

REFERENCES

BENOÎT, E. 1990 *Dynamic Bifurcations* (ed. E. Benoît). Springer.

BUSSE, F. H. 1967 Non-stationary finite amplitude convection. *J. Fluid Mech.* **28**, 223–239.

CHANDRASEKHAR, S. 1961 *Hydrodynamic and Hydromagnetic Stability*. *International Series of Monographs on Physics*, Oxford.

COX, S. M. & MATTHEWS, P. C. 2002 Exponential time differencing for stiff systems. *J. Comput. Phys.* **176**, 430–455.

CROSS, M. C. 1980 Derivation of the amplitude equations at the Rayleigh–Bénard instability. *Phys. Fluids* **23**, 1727–1731.

CROSS, M. C. & HOHENBERG, P. C. 1993 Pattern formation outside of equilibrium. *Rev. Mod. Phys.* **65**, 851–1123.

DAVIS, S. H., MÜLLER, U. & DIETSCHE, C. 1984 Pattern selection in single-component systems coupling Bénard convection and solidification. *J. Fluid Mech.* **144**, 133–151.

FOSTER, T. D. 1965 Stability of a homogenous fluid cooled uniformly from above. *Phys. Fluids* **8**, 1249–1257.

GOLUBITSKY, M., SWIFT, J. W. & KNOBLOCH, E. 1984 Symmetries and pattern selection in Rayleigh–Bénard convection. *Physica* D **10**, 249–276.

HOYLE, R. B. 2006 *Pattern Formation*. Cambridge University Press.

HUPPERT, H. E. 2000 Geological fluid mechanics. In *Perspectives in Fluid Dynamics* (ed. G. K. Batchelor, H. K. Moffatt & M. G. Worster), pp. 447–495. Cambridge University Press.

KUZNETSOV, E. A., NEPOMNYASHCHY, A. A. & PISMEN, L. M. 1995 New amplitude equation for Boussinesq convection and nonequilateral hexagonal patterns. *Phys. Lett.* A **205**, 261–265.

https://doi.org/10.1017/jfm.2011.284 Published online by Cambridge University Press

LANDAU, L. D. & LIFSHITZ, E. M. 1995 *Fluid Mechanics*. Pergamon.

LIU, Y., NING, L. & ECKE, R. E. 1996 Dynamics of surface patterning in salt-crystal dissolution. *Phys. Rev.* E **53**, R4271–R4274.

LYTHE, G. D. 1996 Domain formation in transitions with noise and a time-dependent bifurcation parameter. *Phys. Rev.* E **53**, R5572–R5575.

MAJDALANI, J. 1998 A hybrid multiple scale procedure for boundary layers involving several dissimilar scales. *Z. Angew. Math. Phys.* **49**, 849–868.

MANDEL, P. & ERNEUX, T. 1987 The slow passage through a steady bifurcation: delay and memory effects. *J. Stat. Phys.* **48**, 1059–1070.

MOORE, D. R. & WEISS, N. O. 1973 Nonlinear penetrative convection. *J. Fluid Mech.* **61**, 563–581.

NEWELL, A. C. & WHITEHEAD, J. A. 1969 Finite bandwidth, finite amplitude convection. *J. Fluid Mech.* **38**, 279–303.

SCHLÜTER, A., LORTZ, D. & BUSSE, F. H. 1965 On the stability of steady finite amplitude convection. *J. Fluid Mech.* **23**, 129–144.

SEGEL, L. A. 1969 Distant side-walls cause slow amplitude modulation of cellular convection. *J. Fluid Mech.* **38**, 203–224.

SPIEGEL, E. A. & VERONIS, G. 1960 On the Boussinesq approximation for a compressible fluid. *Astrophys. J.* **13**, 442–447.

SULLIVAN, T. S., LIU, Y. & ECKE, R. E. 1996 Turbulent solutal convection and surface patterning in solid dissolution. *Phys. Rev.* E **54**, 486–495.

WOODS, A. W. 1992 Melting and dissolving. *J. Fluid Mech.* **239**, 429–448.

WORSTER, M. G. 2000 Solidification of fluids. In *Perspectives in Fluid Dynamics* (ed. G. K. Batchelor, H. K. Moffatt & M. G. Worster), pp. 393–446. Cambridge University Press.

https://doi.org/10.1017/jfm.2011.284 Published online by Cambridge University Press